Towards 30% Power Conversion Efficiency in Thin-Silicon Photonic-Crystal Solar Cells

Sayak Bhattacharya, Ibrahim Baydoun, Mi Lin, and Sajeev John

Phys. Rev. Applied **11**, 014005 — Published 3 January 2019

DOI: 10.1103/PhysRevApplied.11.014005

Towards 30% power conversion efficiency in thin-silicon photonic-crystal solar cells

Sayak Bhattacharya,[1,*] Ibrahim Baydoun,[1] Mi Lin,[1,2] and Sajeev John[1]

[1] *Department of Physics, University of Toronto, 60 St. George Street, Toronto M5S 1A7, Ontario, Canada*

[2] *College of Electronic Science and Technology, Shenzhen University, Shenzhen 518060, China*

By direct numerical solution of Maxwell's equations and the semiconductor drift-diffusion equations, we demonstrate solar power conversion efficiencies in the $29\% - 30\%$ range in crystalline-silicon photonic-crystal solar cells. These $3 - 12$ μm thick photonic crystals, consisting of wavelength-scale inverted-pyramid arrays, absorb sunlight considerably in excess of the Lambertian limit due to wave-interference based light-trapping. It is suggested that the resulting optimized balance between bulk-Auger recombination and solar absorption occurs for a silicon thickness of 10 μm, in contrast to previous estimates of over 100 μm. Optimized n^+pp^+ doping profiles involving low $p-$doping throughout most of the bulk and thin n^+ and p^+-doping at the emitter and base regions yield ideal electronic response. For solar absorption restricted to the $300 - 1100$ nm range, we obtain a short circuit current of 42.5 mA/cm^2, an open circuit voltage of nearly 0.8 V and a fill-factor of about 87%, provided that the surface recombination velocities are below 100 cm/s. Including solar absorption in the $1100 - 1200$ nm range through electronic bandgap narrowing and the Urbach optical absorption edge, our wave-interference-based light-trapping enables an additional photo-current density of 1.09 mA/cm^2 for an overall power conversion efficiency of 30%. It is shown that under solar concentration by factors of 20 and 150, the power conversion efficiencies are enhanced to 32.5% and 33.5%, respectively.

* sayak.bhattacharya@utoronto.ca

I. INTRODUCTION

Photovoltaics is vital to the ever-increasing global energy demand. As a competitive source of clean energy on a mass scale, a crucial requirement is low-cost, high-efficiency solar cells. The laws of thermodynamics place a maximum possible solar-to-electrical power conversion efficiency of a single junction $c-Si$ cell under $1-$sun illumination at room temperature of 32.23% [1]. In practice, this efficiency is unattainable due to incomplete absorption of sunlight and unavoidable non-radiative recombination of photo-generated charge carriers. The indirect electronic bandgap of silicon makes it a relatively weak absorber of sunlight in the $800-1100$ nm range. Another important limitation in the case of silicon is non-radiative Auger recombination in the bulk of the solar cell. These two considerations lead to an optimum thickness of silicon based on the balance between adequate solar absorption and low bulk recombination loss. In previous literature [2] this limit has been determined using the concept of Lambertian light-trapping [3]. In this picture, light is described by ray-optics and is not endowed with any wave character. The Lambertian light-absorption limit is defined through a series of assumptions, starting with a randomly rough top surface that exhibits no specular reflection to incoming sunlight and that randomly deflects incoming rays through a $\cos\theta$ probability distribution, where θ is angle that the ray within the bulk silicon makes with respect to the surface normal. The deflected ray then bounces off a perfect back-reflector and returns to the top surface. If the return angle is greater than the critical angle defined by $\sin\theta_c = 1/n$ (where n is the wavelength-dependent real part of the refractive index of silicon), then the light undergoes total internal reflection at the top surface. A simple argument [3] then suggests that, on average, an incoming light ray will undergo n^2 bounces from the back-reflector before escaping through the top surface. Consequently, the average path length of light in the solar cell is $4n^2$ times the actual cell thickness. While this argument is not rigorous, the resulting Lambertian absorption spectrum provides a valuable benchmark for gauging the efficacy of actual light-trapping architectures.

Through detailed consideration of recombination in well-passivated $c-Si$, Richter et al. quantified Auger recombination as a function of dopant density and injection level at $300K$ [4]. Assuming perfect Lambertian light-trapping and neglecting practical issues of front-contact shadowing and sheet-resistance, this Auger model then leads to a practical efficiency limit of 29.43% for a single junction, $c-Si$ solar cell under $1-$sun illumination [2]. This theoretical efficiency limit is attained at the thickness of 110 μm where the optimum balance between Lambertian solar absorption and Auger recombination is realized in undoped $c-Si$. An important assumption behind this efficiency limit is that light-trapping is limited by the ray-optics, Lambertian limit [3]. The optimum thickness of 110 μm is a result of the trade-off between increasing photo-current density with increasing thickness and decreasing open-circuit voltage (V_{OC}) due to further bulk Auger recombination. Real-world solar cells, both present and past, typically absorb sunlight below the Lambertian limit. As a result, previous world-record efficiencies have been attained with silicon thickness considerably greater than 110 μm. The present world-record holding heterojunction interdigitated back contact (HJ-IBC) $c-Si$ cell uses 165 μm thick $n-$type bulk $c-Si$ crystal with donor concentration $N_D = 1.5\times10^{15}$ cm^{-3} [5]. This cell exhibits a conversion efficiency of 26.7%, an open-circuit voltage of 0.738 V and a short-circuit current of 42.65 mA/cm^2

[6]. The loss analysis of the Kaneka-cell shows that under ideal condition, the maximum theoretical efficiency of the cell would be 29.1% in the case of perfect Lambertian light-trapping [5]. Furthermore, due to unavoidable Auger recombination the maximum V_{OC} attainable by any 165 μm-thick cell with $N_D = 1.5 \times 10^{15}$ cm^{-3} is 0.761 V [2, 5]. Therefore, it is impossible for any experimental 165 μm-thick cell, employing Lambertian light-trapping scheme, to surpass these theoretical upper-bounds.

In this paper, we suggest a paradigm shift in achieving the highest possible power conversion efficiencies in silicon solar cells. This involves the fundamental concept that thin-film silicon can surpass the theoretical efficiency limits of thick silicon solar cells. Unlike ray-tracing methods that suggest advantages to cell-thickness beyond 100 μm, we consider the precise solution of Maxwell's equations that properly incorporates wave-interference corrections to the ray-optics picture. In the case of silicon photonic-crystals with microstructure on the scale of the optical wavelength, this leads to a major change in the physical picture of light-trapping and an optimum silicon thickness of close to 10 μm. Wave-interference in thin-silicon photonic crystals enables solar absorption well above the Lambertian limit due to two fundamental effects. The first is the highly non-Lambertian deflection of light-rays entering the top surface. Instead of the $\cos\theta$ distribution, a large fraction of incident light is refracted in directions with group velocity nearly parallel to the interface. This is referred to a "parallel-to-interface refraction" (PIR) [7]. The second effect is magnitude of group velocity, which can be considerably less than the "effective-medium" speed of light. Wave-interference gives rise to what are called "slow-light modes". These two effects are associated with the higher bands of the electromagnetic spectrum in the photonic crystal and lead to a much longer dwell time in a thin-film than anticipated by the Lambertian light-trapping arguments.

Reducing the bulk thickness would not only reduce both extrinsic and intrinsic recombination, but would also cut the production cost of the required high-grade $c-Si$. Moreover, at 10 μm thickness, silicon is flexible and may have broader applications. At the same time, near-perfect photon absorption in the thinner $c-Si$ cells is possible through wave-interference based light-trapping[8, 9]. Harvesting of solar energy through coupling of sunlight into slow photonic modes of ultra-thin $c-Si$ PhCs has been discussed previously with modulated nanowire [10, 11] and slanted conical pore [12] architectures. Arrays of slightly thicker inverted pyramid [13–16] and parabolic pore [17] photonic crystals have also been shown to support PIR and slow optical modes to increase the optical path length and dwell time of the photons resulting in significantly increased absorption. Wave-interference based strong resonances associated with parallel-to-interface refraction (PIR) [7] are particularly significant to absorption enhancement in the $800-1100$ nm wavelength range [17] where $c-Si$ has weak intrinsic absorption. Photonic crystal light-trapping effectively offsets the detrimental aspects of the indirect electronic bandgap of silicon, allowing it to absorb as much sunlight as direct-gap semiconductors. It also holds the key to surpassing the statistical ray-trapping (Lambertian) limit. This opens up a completely new possibility of single junction solar cells with efficiencies exceeding ray-optics based theoretical limit of 29.43%.

Experimental studies [18] have demonstrated close to Lambertian limit light trapping using $35\mu m$-thick macroporous Si absorber. Attempts to theoretically [19] surpass the Lambertian limit have been made using rigorous coupled

wave analysis of photonic crystals. Mode-coupling theory has been used to suggest that conventional limits can be surpassed in nano-photonic structures [20]. External cavities have also been proposed [21] in this context. Through experimental measurements guided by rigorous numerical solution of Maxwell's equations, Kuang et. al. [17] have shown that the absorption of $300-1100$ nm sunlight in a non-optimized 10 μm thick $c-Si$ parabolic-pore PhC with 1200 nm lattice constant, fabricated by reactive ion etching (RIE), results in a maximum achievable photocurrent density (MAPD) close to the Lambertian limit of 39.63 mA/cm^2. Considerably further improvement in this MAPD is expected by optimizing the parabolic-pore height to lattice-constant ratio. Numerical and experimental work using inverted pyramid PhC has shown close to Lambertian limit light absorption in both 5 μm and 10 μm thick $c-Si$ [14]. Rigorous FDTD study (using the Electromagnetic Template Library (EMTL) [22]) of a $1.6\mu m$-thick $c-Si$ slanted conical-pore PhC has shown [12] that it is possible to exceed Lambertian limit over the broad AM1.5G spectrum. Inverted pyramid PhCs, on the other other hand, can be fabricated accurately on a mass-scale by wet-etching. The anisotropic etching property of KOH towards $c-Si$ leads naturally to inverted pyramids with side-wall angle 54.7°, the angle between (111) and (100) plane of $c-Si$. Unlike the classical pyramid arrays with $10\mu m$ base lengths [23] that can be described by ray-optics, we consider the largely unexplored regime of micro-pyramid photonic crystals with wavelength-scale features and novel wave-optics phenomena. Using a rigorous FDTD solution of Maxwell's equations, light-trapping and absorption beyond the Lambertian limit was demonstrated [13] in an optimized 10 μm thick $c-Si$ inverted micro-pyramid PhC. The optimum lattice constant in this case is 2500 nm, yielding a MAPD of 42.5 mA/cm^2.

In a real-world crystalline-silicon cell, optical absorption throughout the wavelength range of $300-1200nm$ is relevant to the generation of charge carriers. Recombination of these carriers is dominated by Auger process and defect-induced trap states in the bulk and at surfaces. In order to isolate the various contributions to solar cell efficiency and make head-to-head comparison with previous literature, we discuss models in which solar absorption in the $1100-1200nm$ range is either included or excluded. We also compare models in which the defect-induced carrier lifetimes are $1.2ms$ or $10ms$. Finally, we isolate the role of the sheet resistance due to lateral carrier transport between widely-separated electrical contact-fingers. This leads a sequence of slightly varying theoretical projections for the power conversion efficiencies with the different models. Nevertheless an overarching conclusion from the various models is that an optimized $10\mu m$-thick $c-Si$ photonic crystal solar cell including the entire available solar spectrum, with state-of-the-art carrier lifetime and sheet-resistance losses included can provide a solar-to-electrical power conversion efficiency of 30%.

In this article, we investigate thin ($3-12$ μm) $c-Si$ solar cells that employ double layer anti-reflection coating (ARC) and wave-interference based light-trapping in carefully optimized inverted pyramid PhCs that surpass the Lambertian limit. We use the MAPDs and absorption profiles obtained by solving Maxwell's equations, as input to the carrier-generation and transport equations for the solar cells. A low doping level (5×10^{15} cm^{-3}) in the $p-$type bulk crystal ensures low bulk Auger recombination. The top and rear of the cell are diffused with highly doped donor and acceptor type impurities, respectively, to form conformal n^+ and p^+ layers at the two ends of the cell.

These provide a front surface field (FSF) and a back surface field (BSF) to deflect minority carriers from the surfaces and contacts. Our electronics design (described in sec. II) is similar to the conventional passivated emitter, rear totally-diffused (PERT) architecture [24–28]. However, due to the reduced Auger recombination in our thin-silicon cell, we predict a power conversion efficiency 5% (additive) higher than the best available PERT cell. Using the optimized doping parameters for FSF and BSF regions (discussed in sec. V and Appendix A), we calculate $J-V$ characteristics of our proposed cells with different thicknesses. While thick cells, in general, absorb more sunlight for higher J_{SC}, the increased non-radiative bulk Auger recombination leads to lower V_{OC}, and lower conversion efficiency (η). We show that 10 μm is the optimum cell-thickness for inverted pyramid PhCs using wave interference-based light-trapping. Considering solar absorption in the $300-1100$ nm wavelength range, our optimum 10 μm thick cell with $N_A = 5\times10^{15}$ cm^{-3} offers $\eta = 29.73\%$ at $25^{\circ}C$ with V_{OC} reaching 0.8 V. This surpasses the hypothetical upper bound of 29.57% based on Lambertian light-trapping in a 110 μm thick cell [2]. Under 20−sun illumination, our thin-silicon cell provides 32.5% efficiency. This efficiency saturates to 33.5% at 150−sun illumination. Including the effects of band gap narrowing (BGN) [29] and phonon-assisted optical absorption in the Urbach optical absorption edge [30–33], we consider further solar absorption in the $1100-1200$ nm range. Our wave-interference-based light-trapping then provides an additional photo-current density of 1.09 mA/cm^2. Despite the slightly reduced V_{OC} of 0.79 V, the overall power conversion efficiency (at one sun) in our 10 μm-thick photonic crystal increases to 30.15%. This suggests a new paradigm for high-efficiency solar cell design beyond the current world record ($\eta = 26.7\%$) using, instead, a flexible 10 μm-thick sheet of $c-Si$.

II. SOLAR CELL DESIGN AND NUMERICAL METHODS

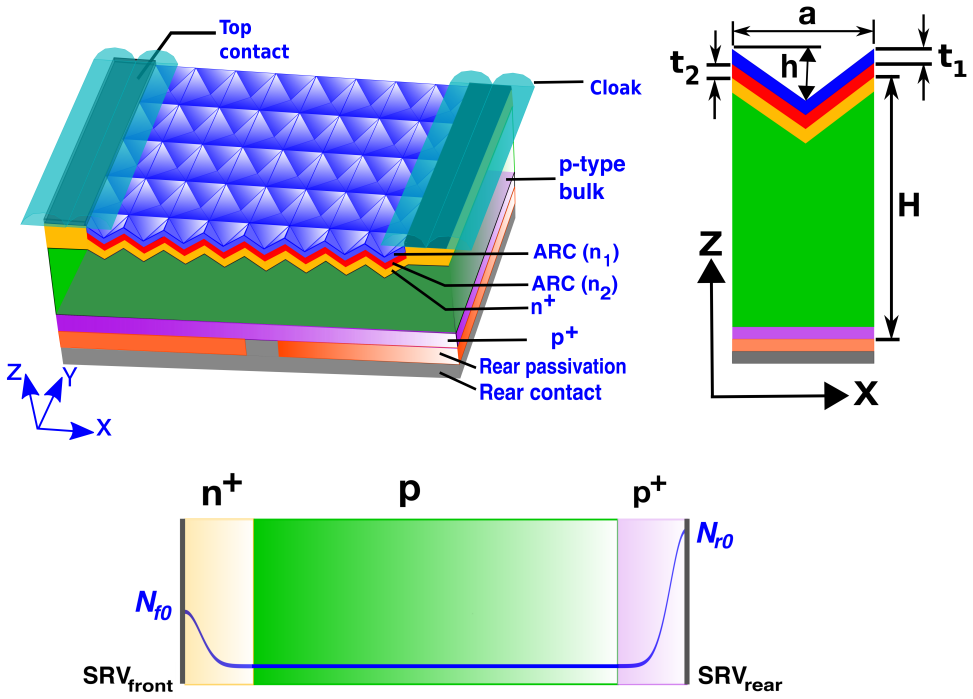

Figure 1. Geometry of inverted pyramid PhC solar cell. Top left: $3D$ view of the cell showing different layers. n_1 and n_2 are the refractive indices of the double layer ARC. Cloaking of top-contact could be a possible way to reduce shading loss [34–37]. Top right: $2D$ cross sectional view of the unit cell of the PhC. The side-wall angle of the wet-etched pyramid is 54.7° (i.e. $h/(a/2) = \tan 54.7^\circ$). The thickness of the active layer is H. Bottom: Equivalent $1D$ model of the solar cell used in the semiconductor carrier transport calculations. The blue line represents the schematic of the doping profile of the cell. N_{f0} and N_{r0} are the peak values of the Gaussian dopings of n^+ and p^+ regions, respectively.

Figure 1 shows the geometry of our inverted pyramid PhC thin $c-Si$ solar cell. The front surface of the $c-Si$ bulk-crystal is textured with a square lattice (photonic crystal lattice constant$= a$) of inverted pyramids. Each pyramid has a side-wall angle $\alpha = 54.7^\circ$, determined by the anisotropic etching of KOH. The height, h, of each pyramid is given by $h = (a/2)\tan\alpha$. The overall thickness of the $c-Si$ active layer is denoted by H. The front surface of the $c-Si$ layer is covered with two conformal ARC layers of refractive indices n_i and thicknesses t_i, where $i = 1$ and 2 correspond to the top and bottom ARC layers, respectively. These two ARC layers also form the front passivation layer for the cell. The front electrode fingers make contact with the $c-Si$ layer through highly doped regions with donor impurities (n^+). The strong electric field between the highly doped, thin n^+ layer and $p-$type bulk keeps the minority carriers (holes) away from the front electrodes, while aiding in efficient collection of the photo-generated electrons. Similarly, the rear p^+ layer acts as the BSF region, aiding in efficient collection of holes. The Gaussian doping profiles of donor and acceptor impurities in the front n^+ and rear p^+ regions are characterized by $N_f = N_{f0}\exp\left(-z^2/2\sigma_f^2\right)$ and $N_r = N_{r0}\exp\left(-z^2/2\sigma_r^2\right)$, where N_{f0} and N_{r0} are the peak donor and acceptor doping concentrations (in cm^{-3}) and σ_f and σ_r are the Gaussian widths (in nm). For the n^+pp^+ cell, the acceptor doping concentration, N_A, throughout the $p-$region is assumed to be 5×10^{15} cm^{-3} in all numerical computations.

The absorbed photon density in the solar cell is computed by finite difference time domain simulation [38], which produces excellent agreement with the experimentally measured absorption spectra of the $c-Si$ PhCs [17]. EMTL provides a stable FDTD scheme for solving Maxwell's equations with accurate modeling of the frequency-dependent dielectric function of Si using modified Lorentz terms [39]. The top right panel in fig. 1 shows the cross section of the unit cell used for FDTD computations. The rear metal contact of the cell is modeled as perfect electric conductor (PEC) and acts as a back-reflector for the sunlight. The rear passivation layer is implemented as a 50 nm SiO_2 ($n = 1.45$) layer. This reduces parasitic absorption losses in real-world back contact such as silver [13] and justifies our modeling of the back-reflector as a PEC. We apply periodic boundary conditions (PBC) along x and $y-$directions and put perfectly matched layers (PML) at the computation boundaries normal to the $z-$direction. The solar cell is illuminated with a normally incident broadband plane wave, coming from $+z-$direction, that has significant energy in $300-1200$ nm spectral range. For FDTD computations neglecting BGN, we calculate the absorbed photon densities in the $300-1100$ nm wavelength range and for those including BGN, we select the upper limit of the wavelength (λ_{max}) to be $1200nm$. This choice of λ_{max} includes two distinct effects. The first one is the electronic band gap narrowing of $c-Si$, denoted by ΔE_g (in eV) and estimated using Schenk's model [29] in our electronic calculations. The second effect, discussed in sec. VI, includes a small amount of additional solar absorption available through the Urbach tail [30, 31] below $(E_g - \Delta E_g)$ due to phonon-assisted absorption [32, 33]. Here E_g is unperturbed electronic bandgap of Si. From FDTD computation, we first calculate the absorption coefficient of the $c-Si$ as $A(\lambda) = 1 - R(\lambda) - T(\lambda)$, where $R(\lambda)$ and $T(\lambda)$ are the reflection and transmission coefficients of the structure. The MAPD of the cell under $AM1.5G$ illumination is given by:

$$J_{MAPD} = \int_{\lambda=300\text{ nm}}^{\lambda_{max}} \frac{e\lambda}{hc} I(\lambda)A(\lambda)d\lambda \tag{1}$$

Here, $I(\lambda)$ is the intensity of the $AM1.5G$ spectrum and it is assumed that each absorbed photon creates a single electron-hole pair. For an ideal cell, without any surface and bulk recombination losses, the short-circuit current J_{SC} coincides with J_{MAPD}.

Based on the absorbed photon density and J_{MAPD} obtained from FDTD calculations, we model electronic response of the $3D$ solar cell by an equivalent $1D$ model (shown in bottom panel of fig. 1). We also verify the accuracy of this $1D$ model by comparison with $2D$ and $3D$ transport calculations. This microscopic $1D$ model enables optimization of the performance of the cell under different doping profiles, bulk recombination profiles and surface recombination velocities. Carrier-transport calculations are carried out with Sentaurus software [40], using SRH lifetimes $(\tau_{SRH}) = 1.2ms$ and $10ms$ as well as state-of-the-art Auger recombination model [4]. An additive efficiency improvement of 0.5% is typically available by increasing τ_{SRH} to $10ms$. The simulation temperature is assumed to be $300K$, except when we compare the performance of our proposed cell with those determined at $25°C$ [2]. Geometric details of the passivation layers and contacts in the $3D$ cell are subsumed into equivalent front and rear surface recombination velocities, SRV_{front}

and SRV_{rear}. These appear in the equivalent $1D$ transport as boundary conditions. In our $2D$ and $3D$ electronic transport models, distinct SRVs are chosen for contacts and insulating surface areas.

The overall solar cell electronic response is dominated by the integrated solar absorption (MAPD) and not strongly influenced by small variations in the spatial profile of absorption. Accordingly we map the exact carrier generation profile obtained by solving Maxwell's equations in the actual $3D$ photonic crystal to the $1D$ electronics model by a simple algorithm. For each optical wavelength we adopt a Beer-Lambert exponentially decaying absorption profile based on the complex, wavelength-dependent dielectric function of $c-Si$. The intensities of these exponentially decaying profiles are set according to the actual $AM1.5G$ solar spectrum. An artificial carrier generation profile is then obtained by integrating these profiles over the $300-1100$ nm wavelength range. An artificial short-circuit current, J_{SC0}, is generated in the $1D$ model using Sentaurus by initially neglecting Auger recombination, choosing τ_{SRH} very large and setting SRV_{front} and SRV_{rear} to very small values. This J_{SC0} (in the absence of losses) is smaller than J_{MAPD} from the $3D$ simulation of Maxwell's equations in the actual inverted pyramid PhC. In order to compensate we rescale the Sentaurus $1D$ generation profile by a factor of (J_{MAPD}/J_{SC0}). This carrier generation profile is used in the subsequent Sentaurus computations that include realistic SRH, Auger and surface recombination. We have verified that this simplified algorithm reproduces with reasonable accuracy the current-voltage characteristic curves obtained from a full-fledged solution of the $3D$ electronic transport equations, using the exact carrier generation profiles derived from Maxwell's equations.

In order to obtain a good convergence for transport calculations with very thin n^+ and p^+ regions, an adaptive meshing strategy is used to ensure at least 20 mesh steps in the n^+ and p^+ regions. To resolve sharp changes in the highly doped regions with total widths less than 100 nm, at least 50 mesh steps are used . Adaptive meshes are denser in the regions where the doping profile changes rapidly and vice versa. In Appendix B, we consider $2D$ carrier transport calculations with the actual carrier generation profile of the inverted pyramid PhC solar cell. Here, the $3D$ carrier generation profile, calculated using FDTD, is integrated along one of the lattice directions. The resulting $2D$ profile is repeated over a very large number of unit cells of the photonic crystal and mapped onto the Sentaurus grid, in order to simulate the effect of contact finger spacing much larger than the photonic crystal lattice constant.

III. INVERTED MICRO-PYRAMIDS AND THEIR OPTIMIZATION

Pyramid and inverted-pyramid [23, 41–45] surface structures have been useful in the design of classic solar cells that have achieved previous world-record efficiencies. These conventional designs utilize architectures with length-scales much larger than the wavelength of light to deflect sunlight in a classical ray-optics picture. In contrast, our inverted micro-pyramid photonic crystals involve length-scales and lattice constants comparable to the optical wavelength. In these "non-classical" inverted pyramids, light propagation must be described using wave-optics and the exact solution of Maxwell's equations. The resulting wave-interference-based light-trapping is considerably more effective than with their classical counterparts.

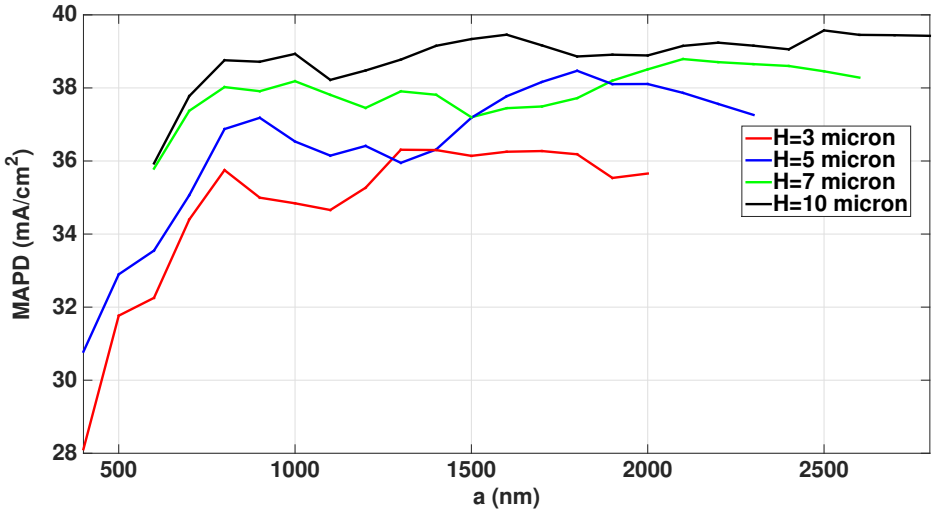

Figure 2. Light-trapping optimization in $3-10\mu m$-thick inverted pyramid photonic crystals (without ARC layer). As the photonic crystal becomes thicker, the optimum lattice size shifts towards higher values.

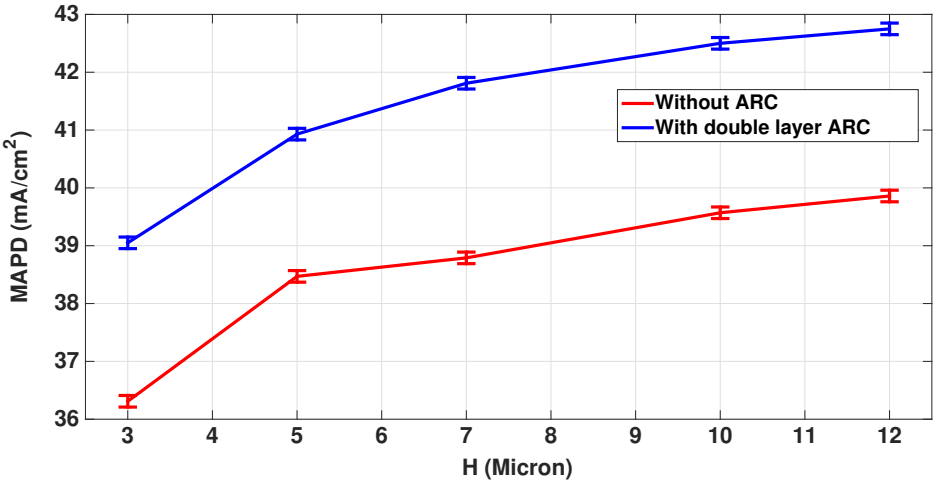

Figure 3. Variation of MAPD in the $300-1100$ nm wavelength range with cell-thickness: Optimization of the refractive indices and widths of the double layer conformal ARC enhances MAPD by $2.5-3$ mA/cm^2. The error bars correspond to ± 0.1 mA/cm^2 uncertainty in the computed MAPDs.

$H(\mu m)$	$a(nm)$	n_1	n_2	t_1 (nm)	t_2 (nm)	MAPD corresponding to Lambertian limit (mA/cm^2)	MAPD in inverted pyramid PhC solar cell (mA/cm^2)
3	1300	1.4	2.6	95	45	36.64	39.05 ± 0.1
5	1800	1.4	2.7	90	40	38.03	40.93 ± 0.1
7	2100	1.4	2.5	100	45	38.85	41.81 ± 0.1
10	2500	1.4	2.6	100	45	39.63	42.50 ± 0.1
12	2700	1.4	2.6	100	45	40.01	42.75 ± 0.1
15	3100	1.4	2.6	100	45	40.44	43.03 ± 0.1

Table I. Summary of optical optimization in the $300-1100$ nm wavelength range, for inverted pyramid PhC solar cells neglecting bandgap narrowing (BGN).

The optimization study for our inverted pyramid PhC based solar cell starts by identifying the optimum lattice constants for different cell-thicknesses. Figure 2 shows the optimization results for $H = 3$, 5, 7 and 10 μm in absence of ARC layer. The corresponding optimum lattice constants are obtained as $a = 1300$, 1800, 2100 and $2500nm$, respectively, with MAPDs 36.31, 38.47, 38.79 and $39.57mA/cm^2$. With increasing cell-thickness the optimum value of the lattice constant shifts towards higher values. Next, we optimize the refractive indices and thicknesses of the ARC layers. Table I summarizes the results of our optical optimization. Fig. 3 compares the optimum MAPD variation against cell-thickness for PhC solar cells with and without the optimum ARC layers (described in tab. I). This shows that the double layer ARC significantly increases the MAPD (by $\sim 2.5 - 3$ mA/cm^2) of the inverted pyramid PhC solar cells.

We associate some error margins to the MAPDs obtained from our time-domain numerical calculation that require careful consideration of narrow resonances to ensure accurate convergence. Sharp resonances lead to long-time temporal oscillations before complete absorption takes place. On the other hand, MAPD in an actual experiment may be higher than the ones we predict numerically. Fabrication-induced imperfections tend to smooth out very sharp resonances and the temporal oscillations in the long wavelength range of the absorption spectra. This smoothening of the sharpest resonances can be simulated numerically by choosing a coarser frequency resolution, in other words, a shorter simulation duration.

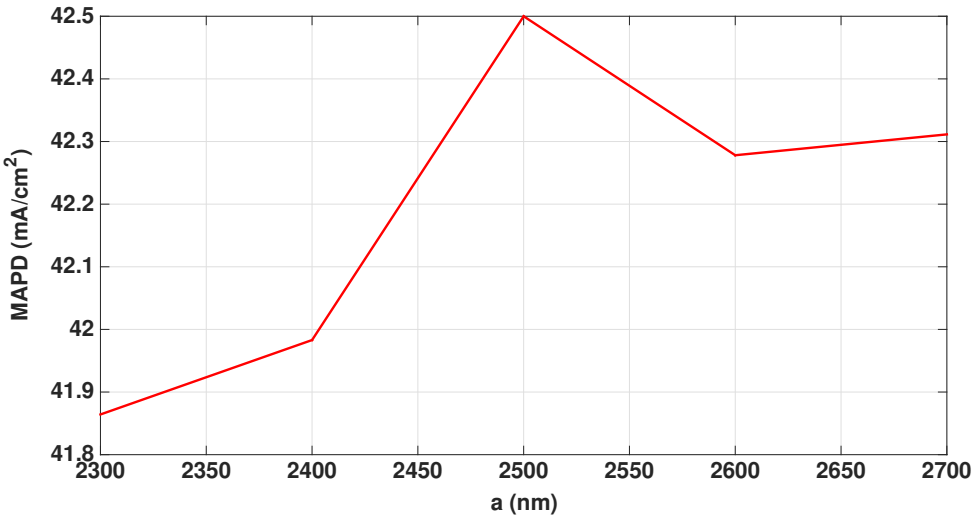

Figure 4. MAPD variation of the AR coated $10\mu m$-thick cell with lattice constant. The parameters for the dual layer ARC are: $n_1 = 1.4$, $n_2 = 2.6$, $t_1 = 100nm$, $t_2 = 45nm$. For a $\pm 200nm$ variation of lattice constant around the optimum value of $2500nm$, the MAPD reduction is less than $0.64mA/cm^2$.

Figure 4 illustrates the change of MAPD of the optimized, dual-ARC coated $10\mu m$-thick inverted pyramid PhC cell with respect to small variation Δa in lattice constant around the optimum value of $2500nm$. For $0 < \Delta a < 200nm$, the drop in the MAPD is no more than $0.22mA/cm^2$, whereas for $-200nm < \Delta a < 0$, the MAPD drop is no more than $0.64mA/cm^2$. For $a < 2400nm$ the MAPD drops more slowly. As seen in fig. 2, the $10\mu m$-thick structure without ARC exhibits very high MAPD for lattice constants as small as $800nm$. The MAPDs at $a = 1000nm$ and $a = 1600nm$ are only slightly below the absolute maximum value at $a = 2500nm$. Clearly, our optimized PhC structure exhibits high tolerance to moderate lattice variations and disorder.

Other possible sources of decrease in MAPD in a real-world cell are off-normal incidence of light and encapsulation with glass or ethylene vinyl acetate (EVA). Numerical results presented in [12] have shown that PhC solar cells, in general, exhibit excellent angular response up to an off-normal angle of incidence of 50° without substantial degradation of MAPD. The PIR modes of the PhC are excited with light incident within a 50° cone around the normal [7]. Standard EVA/glass encapsulation reduces the MAPD of the PhC. However, it has been shown in [46] that for lattice constants larger than $1000nm$, an additional $130nm$-thick layer of planar ARC, with a refractive index of 1.27, on the top of EVA/glass enables similar or better anti-reflection performance as compared to the original air-ARC-PhC system.

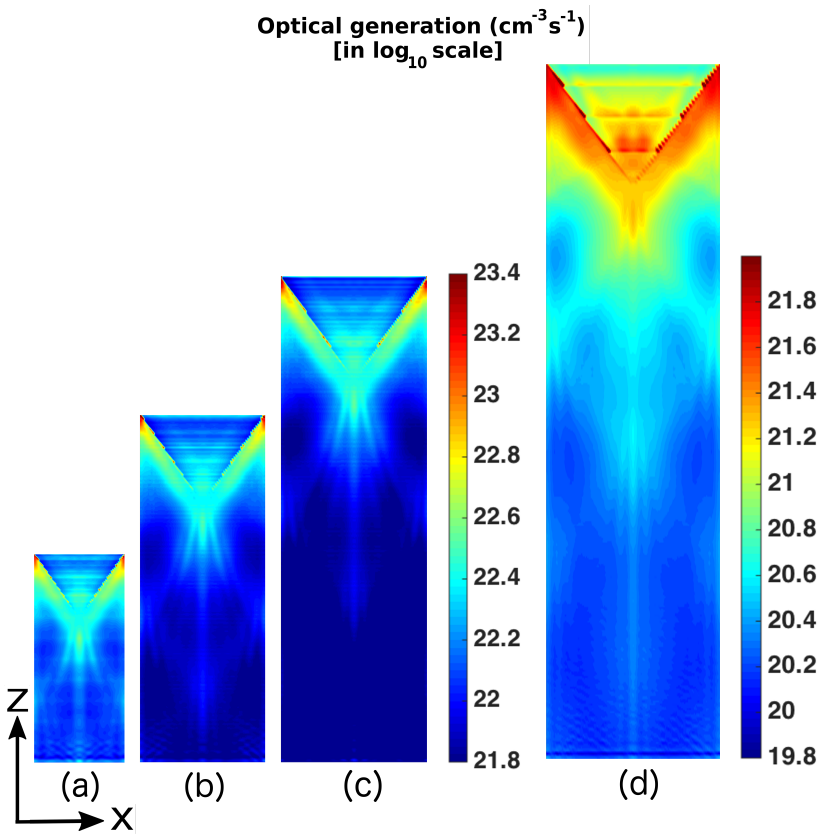

Figure 5. Carrier generation rate within the unit cell of various inverted pyramid PhC solar cells (integrated along y-direction): (a) $H = 3\mu m$, $a = 1300nm$, (b) $H = 5\mu m$, $a = 1800nm$, (c) $H = 7\mu m$, $a = 2100nm$ and (d) $H = 10\mu m$, $a = 2500nm$. The lattice constants correspond to optimized PhCs. In $3D$, thin wedges of silicon occur within the triangles, leading to carrier generation throughout the depicted $2D$ regions.

The carrier generation rates within the $c-Si$ region of various inverted pyramid PhC solar cells are shown in fig. 5. The $3D$ carrier generation rate within the PhC unit cell is integrated along one lattice direction ($y-$direction, in this case). The triangular regions at the top of the generation profiles have an approximate side-wall angle of $54.7°$. Fig. $5(a)$, (b) and (c) show the carrier generation rates for optimized $3, 5$ and $7\mu m$-thick cells, respectively. Although the optimum lattice constants are different for cells with $H = 3, 5$ and $7\mu m$, the carrier generation profiles exhibit very similar distributions. For the optimum $10\mu m$-thick cell with $a = 2500nm$ the peak carrier generation rate (shown in fig. $5d$) is smaller by more than an order of magnitude in comparison to the thinner cells but the peak generation region near the top of the cell is more extended.

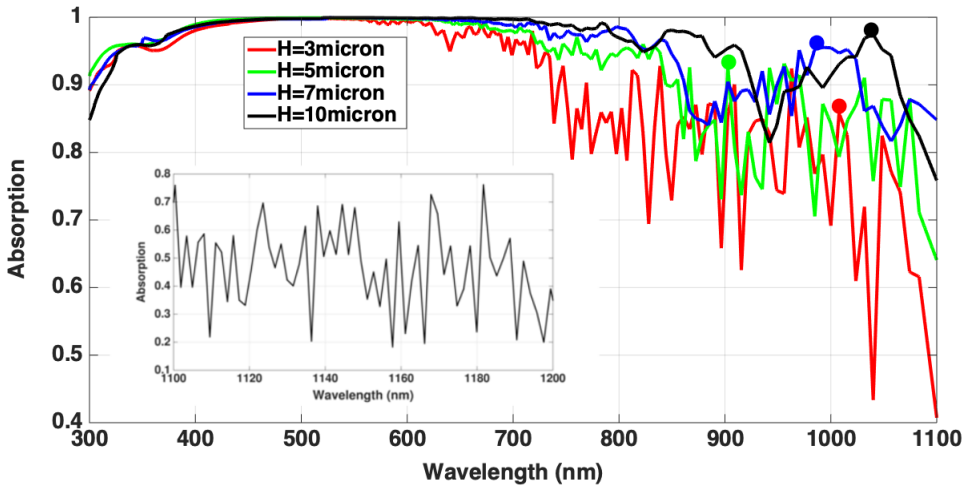

Figure 6. Absorption spectra of inverted pyramid PhC $c-Si$ solar cells with $H = 3$, 5, 7 and 10 μm over the $300-1100$ nm wavelength range. Inset shows the $(1-R-T)$ of the 10 μm PhC over the $1100-1200$ nm wavelength range, used in computations that involves BGN and the Urbach tail. The PhCs are assumed to have optimized double layer ARC given in table I. The solid circles indicate sample resonances with PIR and vortex-like energy flow, shown in fig. 8.

Figure 6 plots the absorption spectra of the optimized inverted pyramid PhC solar cells with thicknesses ranging over $3-10\mu m$. The inset shows the sub-band absorption (over the $1100-1200nm$ wavelength range) in the $10\mu m$-thick inverted pyramid PhC cell. A detailed discussion of the sub-band absorption appears in sec. VI.

In this paper we consider only the optimization with respect to inverted pyramid lattice constant and antireflection coating. Additional optimization can be performed through the shaping of the lower contact protrusions that touch the p^+ doping layer through gaps in the bottom SiO_2 passivation layer. For example, it has been shown [47] that with an ultra-thin active layer thickness of $H = 1.6$ μm, plasmonic resonances in the lower contact can lead to MAPD of 38 mA/cm^2.

IV. COMPARISON OF LAMBERTIAN AND WAVE-INTERFERENCE-BASED LIGHT-TRAPPING

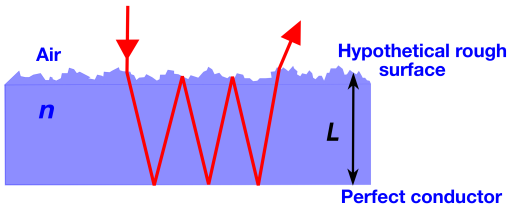

Figure 7. Statistical ray-trapping in a slab. Slab with thickness L and refractive index n. Randomly rough, hypothetical top surface with zero specular reflection for all incoming rays and perfect total internal reflection for rays within the slab incident at an angle greater than the critical angle. The slab is placed on a perfect reflector.

As shown in table I, the thin-silicon PhC solar cells are able to achieve MAPDs exceeding the upper-bounds suggested by statistical ray-trapping [12, 48]. In order to gain physical insight into how light-trapping capability of our optimized PhCs exceeds that of ray optics, we briefly discuss the underlying assumptions of the Lambertian

limit. The geometry associated with the ray-optics picture is depicted in fig. 7. We assume that the thickness and refractive index of the ray-trapping slab are L and n, respectively. The bottom surface of the slab is assumed to be perfectly reflecting and the rough top surface has three hypothetical properties: (i) The surface causes no specular reflection of the light-rays incident from air. (ii) It allows perfect escape of light from the slab incident at an angle less than the critical angle, θ_c (given by $\sin\theta_c = 1/n$), with respect to surface normal and causes total internal reflection otherwise. Thus, the incident rays within a cone of angle θ_c are allowed to escape. (iii) The surface redirects both the externally incident light and total internally reflected light randomly at an angle θ with respect to the normal in the slab according to a probability distribution $f(\theta)$. The probability p that the light inside the slab escapes into air is given by the fraction of rays lying within the solid angle formed by the cone of angle θ_c and can be written as:

$$p = \int_0^{2\pi} d\phi \int_0^{\theta_c} \sin\theta f(\theta) d\theta \tag{2}$$

In case of a Lambertian surface, $f(\theta) = \frac{1}{\pi}\cos\theta$, $0 \leq \theta \leq \pi/2$ [49]. For such surfaces, eqn. 2 yields $p = 1/n^2$. From properties (ii) and (iii), rays can undergo multiple bounces within the slab before escaping. Let m be the number of times a ray traverses the distance $2L$ and $G(m)$ be the probability of making m traversals before escaping. Clearly, $G(1) = p$. Also, $G(m) = p(1-p)^{m-1}$ since, the ray does not escape in the first $(m-1)$ traversals and finally escapes in the m^{th} traversal. So, the average number of traversal is given by, $< m >= \sum_{m=1}^{\infty} mG(m) = 1/p$. Since the ray is reflected at an angle θ after each total internal reflection, the path-length within the slab is given by $2L/\cos\theta$. The average path-length in a single traversal can be written as:

$$L_{avg} = \int_0^{2\pi} d\phi \int_0^{\theta_c} \sin\theta f(\theta) \frac{2L}{\cos\theta} d\theta \tag{3}$$

For a Lambertian surface the above integral yields $L_{avg} = 4L$. Thus, the overall path-length can be calculated as $L_{trap} = L_{avg} < m >= 4n^2 L$, yielding the $4n^2$ enhancement factor. However, PhCs exhibiting PIR modes deviate dramatically from the Lambertian probability distribution and exhibit significant probability of ray-propagation close to $\theta = 90°$. Direct numerical solution of Maxwell's equations shows that our PhC structure has multiple parallel to interface resonances in the $800 - 1100nm$ wavelength range. Moreover, these slow-light modes with multiple internal bounces and vortex-like energy circulation differ drastically from simple rays of light. PIR and vortex-like modes together increase the effective optical path-length by a factor much greater than $4n^2$, yielding MAPD that exceeds Lambertian limit. We demonstrate the existence of such resonances and rich energy-flow pattern within the inverted pyramid PhC in figs. 6 and 8.

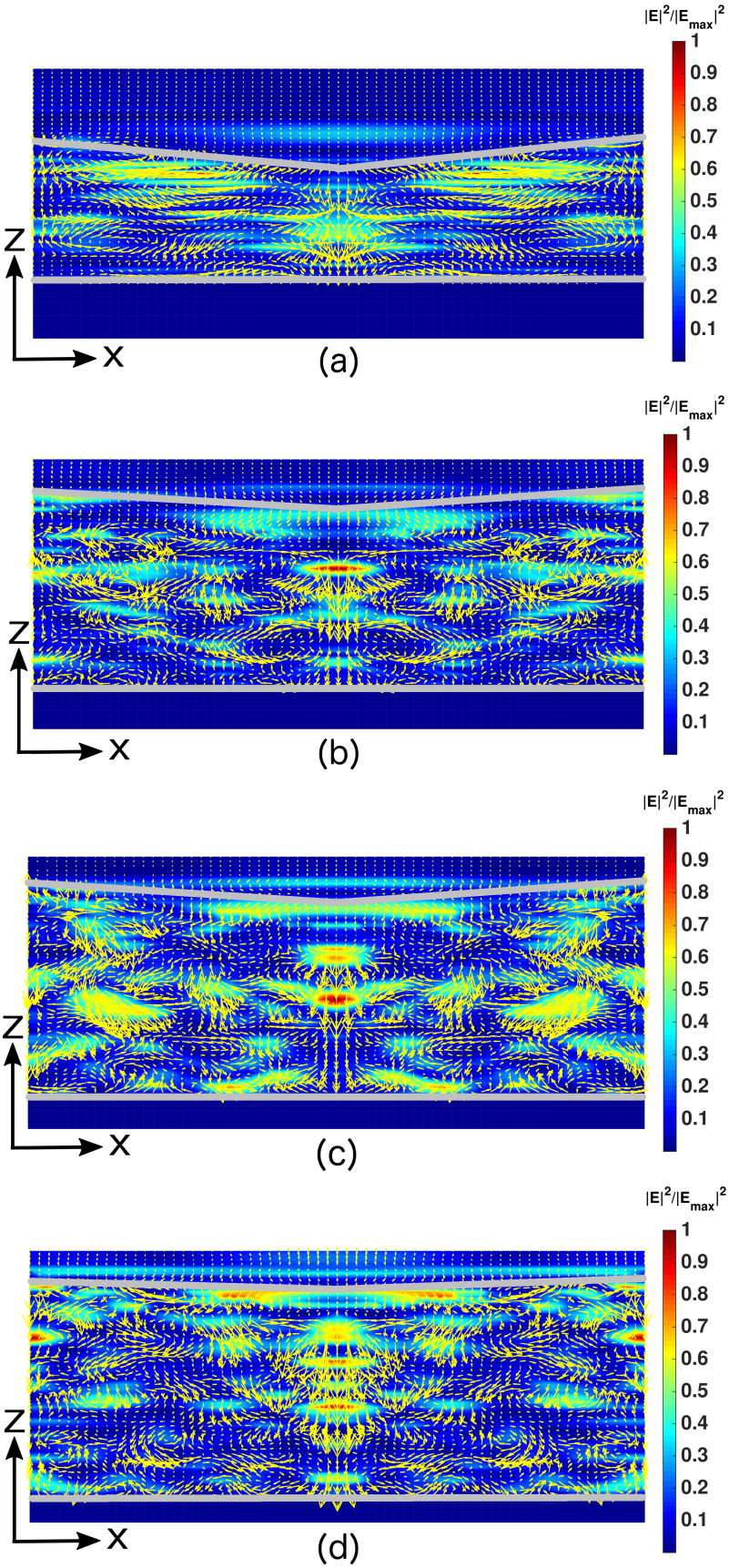

Figure 8. Parallel to interface and vortex-like energy flow in the slow-light modes of the inverted pyramid PhC. The plot shows in-plane Poynting vector flow corresponding to the central xz-plane of the PhCs: (a) $H = 3\mu m$, $\lambda = 1008nm$, (b) $H = 5\mu m$, $\lambda = 902nm$, (c) $H = 7\mu m$, $\lambda = 986nm$ and (d) $H = 10\mu m$, $\lambda = 1040nm$. The colormaps show the normalized electric-field intensity. The boundary of the $c - Si$ substrate is denoted by white line. The aspect ratio of the structure is altered to show the Poynting vectors clearly. However, the aspect ratios of the arrows are not altered and their relative lengths at a given point denote the total magnitude of x and z-components of Poynting vector at that point.

The solid circles on the absorption spectra in fig. 6 identify typical resonances that give rise to strong solar light absorption through coherent light-scattering and interference based effects such as, parallel-to-interface and vortex-like propagation of light within the PhC. Figure 8 illustrates such effects for optimized PhCs with $H = 3, 5, 7$ and $10\mu m$ through plots of in-plane component of Poynting vector at the resonances marked by solid circles in fig. 6 ($\lambda = 1008, 902, 986$ and $1040nm$, respectively). The plot-planes in fig. 8 correspond to the xz-slice passing through the center of the PhC unit cell. As shown in fig. 8 (a), (b) and (c), the $3, 5$ and $7\mu m$-thick PhCs exhibit multiple regions with both vortex-like light flow and light flowing purely along x-direction. Figure 8 (d) shows that for $10\mu m$-thick PhC, with an optimum lattice constant of $2.5\mu m$, the PIR effect is obscured by the dominant optical vorticity. These PIR and vortex-like resonances arising from wave-interference clearly show that the inverted micropyramid PhC cannot be accurately described by ray-optics.

V. ELECTRONIC OPTIMIZATION

We now analyze the electronic performance of our PhC solar cell using the equivalent carrier generation profiles obtained through the procedure outlined in sec. II along with the MAPDs in table I. With this input generation profile, we perform the optimization of the Gaussian doping profiles of the n^+ and p^+ regions that result in the best possible conversion efficiency of the 10 μm PhC cell.

We first consider the case without BGN [29] in which only optical absorption from the $300 - 1100nm$ range is included. We then consider the more realistic situation where both BGN and the Urbach optical absorption edge [30–33] contribute to optical generation throughout the entire $300 - 1200nm$ range.

We show that sheet-resistance losses in highly-doped region near the front metallic contacts lead to a slight modification of the doping profile optimization. For reference, we also include calculations (Appendix A) that neglect this sheet resistance in order to make direct comparison with previously published hypothetical Lambertian cells [2]. Finally, we present a validation of our $1D$ transport model by comparing it to exact solutions of the $2D$ and $3D$ semiconductor drift-diffusion equations using the exact optical generation profiles obtained from Maxwell's equations.

A. Sheet Resistance

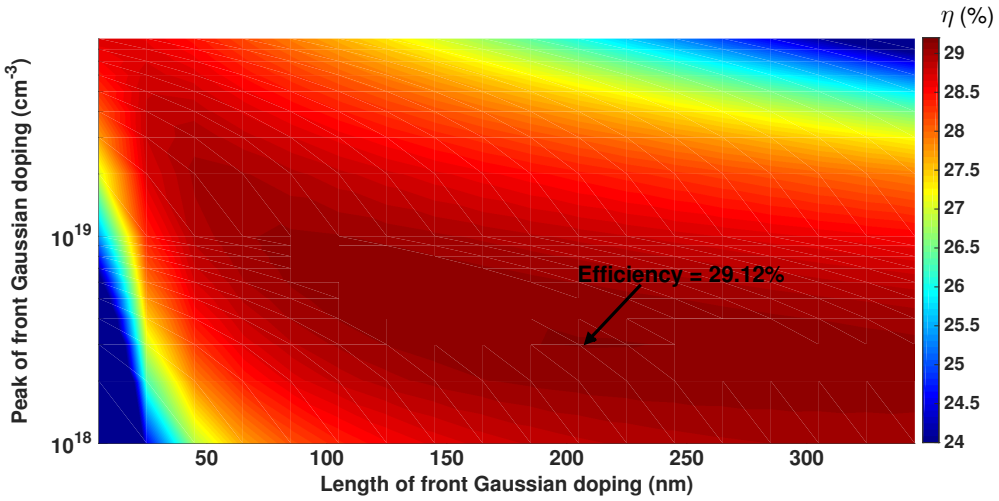

Figure 9. Emitter optimization including sheet-resistance: a maximum efficiency of 29.12% is obtained for $N_{f0} = 3\times10^{18}$ cm^{-3} and $\sigma_f = 205$ nm (equivalent to an emitter width of 730 nm and sheet-resistance of $362\Omega/sq$). The finger-spacing of the top contact has been assumed to be 800 μm (same as 25% PERL cell [50]). Here we assume a MAPD of 42.5 mA/cm^2 arising from solar absorption in the $300-1100$ nm wavelength range, $\tau_{SRH} = 1.2ms$ and the temperature is taken to be $300K$.

In the top-contact solar cell we consider, photo-generated carriers must flow a considerable lateral distance to reach one of the metallic contact fingers. This lateral flow of current through the narrow emitter results in what is known as sheet-resistance. This is automatically accounted for in a $2D$ or $3D$ transport model. In order to quantify the effect of sheet resistance in the simplified $1D$ transport model, we calculate the power-loss (P_{loss}) in the emitter as a fraction of the generated power P_{gen} [51]. We assume initially, a top-contact finger-spacing of 800 μm as deployed in the 25% efficient PERL cell [50]. The actual efficiency of the cell is given by $\eta_{actual} = \eta\,(1 - {}^{P_{loss}}/_{P_{gen}})$. The fraction of power lost, ${}^{P_{loss}}/_{P_{gen}}$, due to the sheet resistance can be calculated as [51]:

$$\frac{P_{loss}}{P_{gen}} = \frac{\rho_{\square} S^2 J_{MP}}{12 V_{MP}} \tag{4}$$

Here, $\rho_{\square}$ =sheet resistance, S =distance between emitter grid lines, J_{MP} and V_{MP} are current density and voltage at the maximum power point of the $J-V$ curve, respectively. The sheet-resistances for different N_{f0} and σ_f are calculated using PV Lighthouse sheet-resistance calculator [52]. Increased emitter width and N_{f0} leads to a lower sheet-resistance but results in higher Auger recombination. Using the $1D$ transport model, a maximum efficiency of 29.12% is achieved (as shown in fig. 9) for $N_{f0} = 3\times10^{18}$ cm^{-3} and $\sigma_f = 205$ nm (equivalently, an emitter-width of 730 nm and a sheet-resistance of 362 Ω/sq). Overall, these considerations of sheet resistance near the upper contact lead to a very small drop in power conversion efficiency by 0.47%, relative to the situation where sheet-resistance is neglected (see Appendix A). Our calculations in Appendix B involving $2D$ and $3D$ transport models, show that this approach provides reasonable agreement with more microscopic treatments of the same effect.

B. Surface Recombination in the $1D$ Transport Model

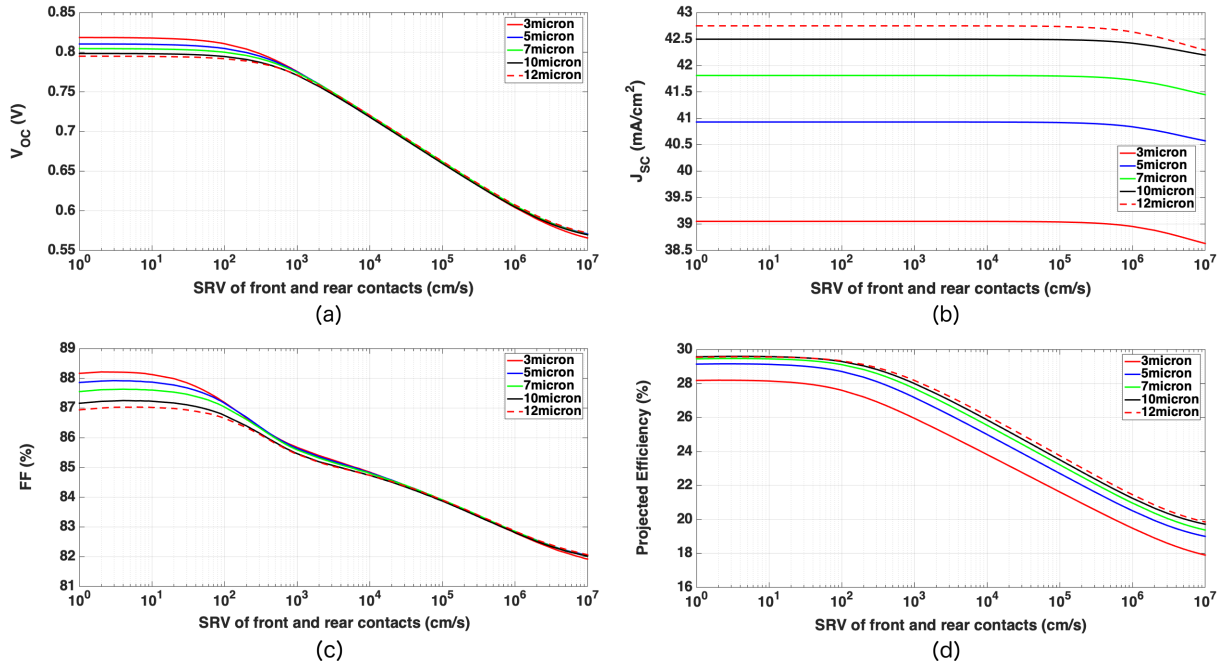

Figure 10. Sensitivity of the performance parameters of optimized $3-12$ μm thick, inverted-pyramid, PhC solar cells to changes in SRV of the front and rear contacts, (at $27^{\circ}C$) using optimized $n^{+}pp^{+}$ doping profiles and $\tau_{SRH} = 1.2ms$. Here solar absorption is restricted to the $300-1100$ nm wavelength range and all calculations are performed with a $1D$ transport model in absence of sheet resistance. Here the front and back surface fields of the n^{+} and p^{+} regions considerably mitigate the effects of surface recombination.

As mentioned in sec. II, the detailed geometries of the passivation layer, contacts etc. are subsumed into SRV_{front} and SRV_{rear} in the $1D$ model and appear as boundary conditions to the semiconductor drift-diffusion equations. Since the quality of the contacts and passivation layers affects the performance of the solar cell, we depict in figure 10 the variation of the performance parameters of our inverted micropyramid $n^{+}pp^{+}$ cells with SRVs of the front and rear contacts. The short-circuit current of the $n^{+}pp^{+}$ cell remains constant over a wide range of SRVs due to the strong FSF and BSF of the optimized n^{+} and p^{+} regions.

An important distinction arises between the solar cell properties depicted in fig. 10 for $SRV > 10^{3}cm/s$ and poorly-passivated solar cells. In our case, the FSF and BSF are part of the passivation and offset the effects of the high SRV. In contrast, a poorly-passivated cell is represented without a separate FSF or BSF, but all near surface recombination is described using an overall effective SRV. The results from such an overall effective SRV are depicted in fig. 11 where it is seen that solar cell efficiency degrades much more dramatically. We fix the $p-$type uniform bulk doping to $2 \times 10^{17}cm^{-3}$ (the optimized bulk doping corresponding to fig. 19). The blue curve shows that if BSF is absent and a non-optimized FSF doping profile is used, the conversion efficiency degrades more rapidly.

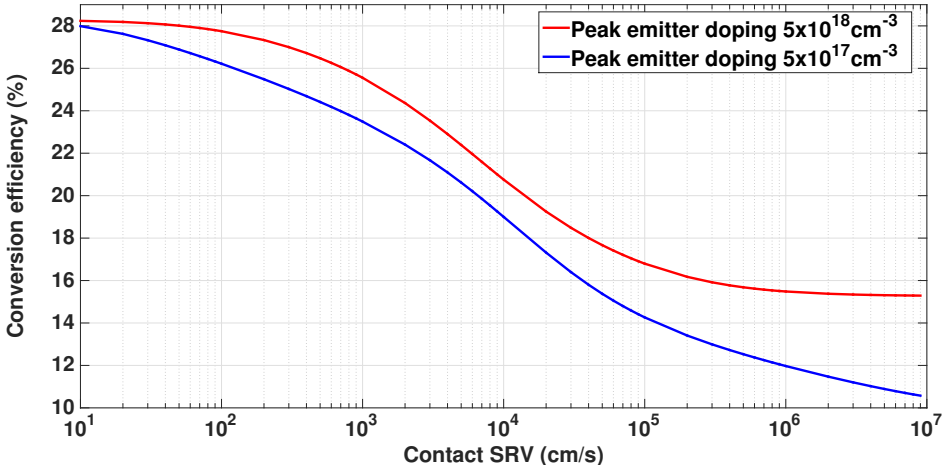

Figure 11. Dependence of conversion efficiency of a $10\mu m$-thick n^+p cell on SRV. Red curve: n^+ emitter has a Gaussian doping with peak concentration $5 \times 10^{18} cm^{-3}$. Blue curve: Peak n^+ doping concentration is $5 \times 10^{17} cm^{-3}$ with no back surface field. In both cases, the $p-$type bulk has a uniform doping concentration of $2 \times 10^{17} cm^{-3}$ and the emitter regions are $20nm$ thick. The red curve corresponds to the optimum doping shown in fig. 19. In both cases, the absence of a back surface field leads to more rapid degradation of the efficiency with SRV. For the blue curve, the degradation is more due to non-optimized emitter doping. For both cases, $\tau_{SRH} = 1.2ms$ and BGN is excluded. Both curves were generated using a $1D$ transport model prior to sheet resistance correction.

The cells described in fig. 10 remain under low-level injection at short-circuit leading to very little change in bulk recombination. Under short-circuit conditions, almost all the generated carriers are collected even when the quality of the contact passivation degrades. On the other hand, V_{OC} of the cell remains almost constant only until $SRV_{front} = SRV_{rear} = 100$ cm/s. For thinner cells, both V_{OC} and the fill-factor exhibit relatively faster variation as compared to thicker cells. Overall, for $H \geq 10$ μm, the conversion efficiency of our n^+pp^+ PhC cell exhibits negligible variation with SRV over $1 - 100$ cm/s SRV range.

C. Cell Thickness Optimization

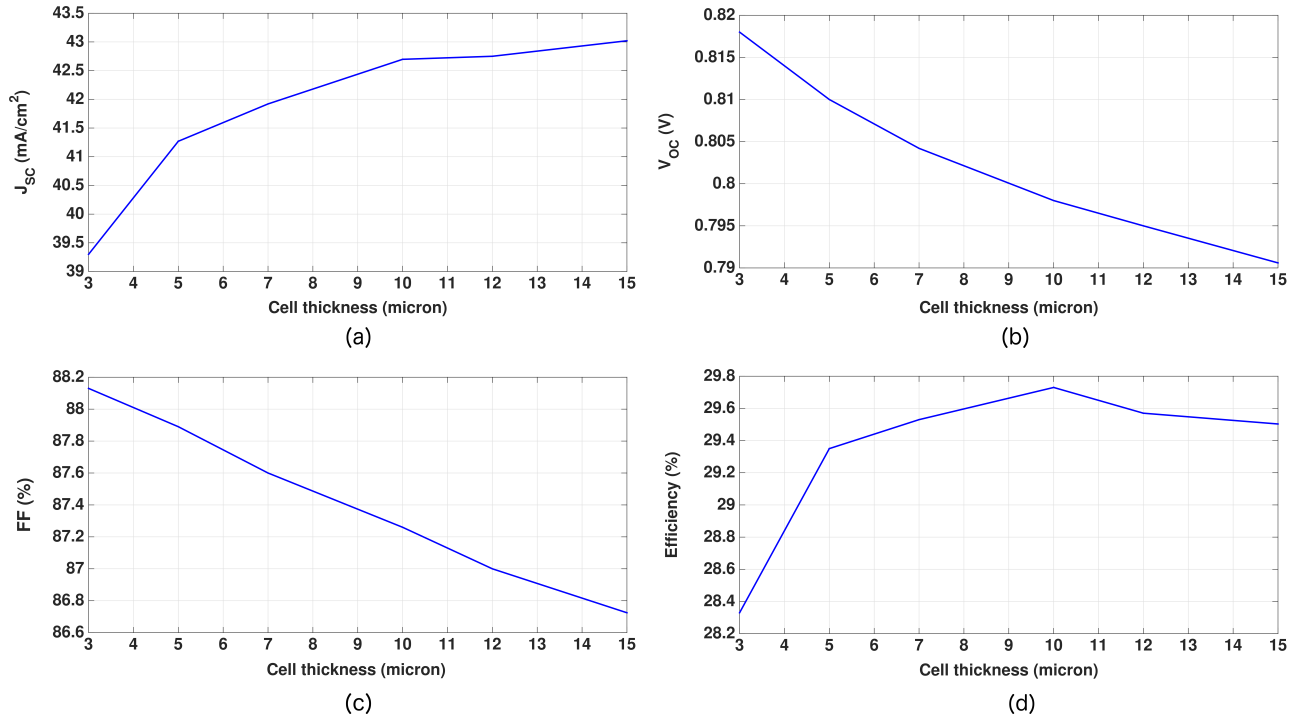

Figure 12. Thickness optimization of inverted pyramid PhC solar cell using the optimized n^+pp^+ doping profile and $\tau_{SRH} = 1.2ms$ at a temperature of $300K$ and restricting solar absorption to the $300 - 1100$ nm wavelength range. These curves were generated using a $1D$ electronic transport model neglecting sheet resistance losses.

In general, a thicker cell can absorb more light, leading to a higher J_{SC}. On the other hand, increased bulk recombination in a thicker cell leads to a lower V_{OC}. The optimum value of H for maximum conversion efficiency is drastically reduced from that suggested by the Lambertian light-trapping picture. Figure 12(a) and (b) show the variation of J_{SC} and V_{OC} with H. As H increases from 3 to 15 μm, the V_{OC} decreases from 818.5 to 791 mV. The fill factor exhibits a relatively small drop from 0.882 to 0.867 as seen in fig. 12(c). As shown in fig. 12(d), our inverted micro-pyramid PhC solar cell has an optimum thickness of 10 μm with 29.59% power conversion efficiency at $300K$. At $25°C$, our optimum cell, with light bulk doping and heavy doping at the ends, exhibits 29.73% efficiency as compared to a hypothetical 110 μm-thick Lambertian light-trapping cell [2] with 29.57% efficiency at $25°C$. The $J - V$ characteristic of our 29.73% efficient optimum cell, based on wave-interference light-trapping, is shown in fig. 13 (blue curve). This corresponds to $V_{OC} = 0.801$ V, $J_{SC} = 42.5$ mA/cm^2 and $FF = 87.33\%$. In this cell-thickness optimization study, all the cells are assumed to have optimized MAPD and optimized design parameters as given in table I.

VI. BANDGAP NARROWING AND THE URBACH OPTICAL ABSORPTION EDGE

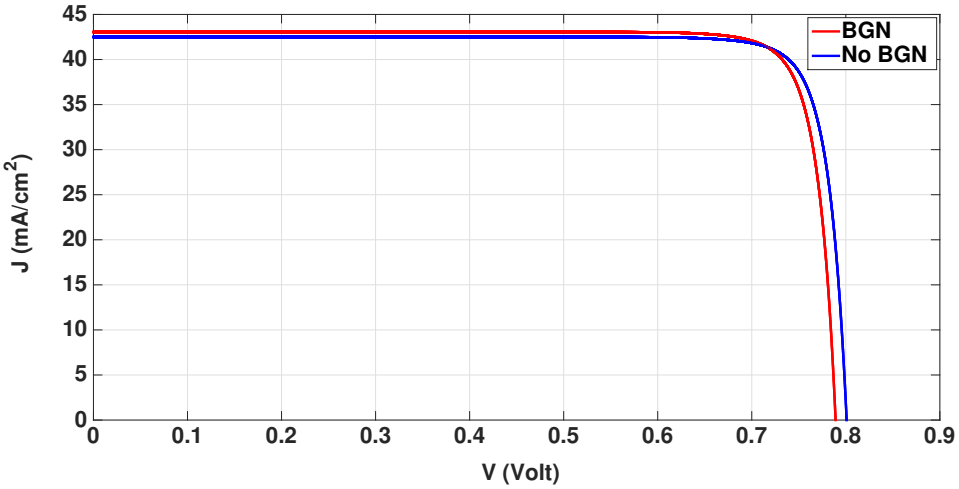

Figure 13. $J-V$ characteristics of 10 μm thick optimized inverted pyramid PhC solar cell with and without bandgap narrowing (BGN) at a temperature of $25°C$. For the blue curve, solar absorption is restricted to the $300-1100$ nm wavelength range, yielding $Jsc = 42.5$ mA/cm^2, $V_{OC} = 0.801$ V, $FF = 87.33\%$ and power conversion efficiency of 29.73%. The red curve includes solar absorption throughout the $300-1200$ nm range to include BGN (shift of the continuum edge) and the Urbach tail in $c-Si$ (due to phonon-assisted generation of electron-hole pairs), yielding $J_{SC} = 43.59$ mA/cm^2, $V_{OC} = 0.7894$ V, $FF = 87.25\%$, and overall power conversion efficiency of 30.02%. In both cases, an optimized n^+pp^+ doping profile is assumed with surface recombination velocities of 10 cm/sec and $\tau_{SRH} = 1.2ms$. This comparison is obtained in a $1D$ electronic transport model without sheet resistance corrections.

We now consider the effect of band gap narrowing (BGN) in our n^+pp^+ cell. BGN is driven by the excess carrier concentration in our cell that is large compared to the doping concentration. In Schenk's model [29], BGN is dependent on the total carrier concentration. Employing Schenk's model in our Sentaurus computations, we estimate ~ 14 meV lowering of the continuum absorption edge. This enables solar absorption for wavelengths as long as 1115 nm in $c-Si$. For conventional solar cells (without wave-interference based light-trapping), BGN offer little advantage since planar $c-Si$ absorbs negligible sunlight in the long wavelength range. At the same time, lowering of the optical absorption continuum reduces the open-circuit voltage of the cell. For example, BGN causes 0.13% efficiency drop in the hypothetical Lambertian solar cell [2]. In contrast, our inverted micro-pyramid PhC solar cell supports wave-interference based slow-light modes and other optical resonances [7] in the long wavelength regime. The incident light is refracted almost parallel to the solar cell surface, further increasing the path-lengths of the long-wavelength photons in the active layer. In the presence of BGN, these trapped photons with long dwell-time eventually get absorbed in $c-Si$. In our 10 μm-thick n^+pp^+ cell with inverted pyramid PhC, a 14 meV band gap narrowing translates into 0.27 mA/cm^2 gain in MAPD. On the other hand, external quantum efficiency (EQE) measurements show that $c-Si$ solar cells are capable of collecting carriers generated by light absorption up to 1200 nm [25–28, 56, 57]. This is more than numerical computations that suggest absorption up to ~ 1120 nm based on BGN. Calculations by Zhao et. al. [25] likewise show a steep cut-off approximately at 1120 nm. This disagreement between the numerical computation

and measurement likely stems from the fact that even $c-Si$ exhibits an exponentially decaying Urbach optical absorption edge below the continuum band edge [30, 31]. Static disorder in non-crystalline solids is well-known to contribute an exponential band tail of localized states below the electronic band edge. However, in $c-Si$ a similar tail of phonon assisted optical absorption gives rise to electron-hole pairs that are mobile [32, 33]. The sub-gap absorption takes the form of an exponential: $\alpha(\nu) \sim exp\,[\{h\nu - E_G(T)/E_0(T)\}]$, where ν is the optical frequency, $E_G(T)$ is the downshift of the continuum band edge corresponding to BGN and $E_0(T)$ is the Urbach slope. Cody et. al. measured the Urbach slope of $c-Si$ at $300K$ as 8.5 ± 1.0 meV. Microscopic modeling of the optical-absorption edge due to both acoustic and optical phonons predicts a slope of 8.6 meV [32, 33]. The inset of fig. 14 shows that the experimental absorption coefficient from [58] exhibits an Urbach slope of 8.6 meV over $1160-1190$ nm wavelength range.

Wavelength range	ϵ_∞	$\triangle\epsilon_j$	$\omega_{pj}(\times 10^3 \mu m^{-1})$	$\gamma_j(\times 10^3 \mu m^{-1})$
$1000-1200$ nm	1.0	0.971156	0.001805	0.000000
		7.244785	0.006785	0.000001
		0.000580	0.001018	0.000047
		2.519084	0.002291	0.000000
		-0.057262	0.001237	0.000004

Table II. Fitting parameters used to fit Si dispersion data of [58].

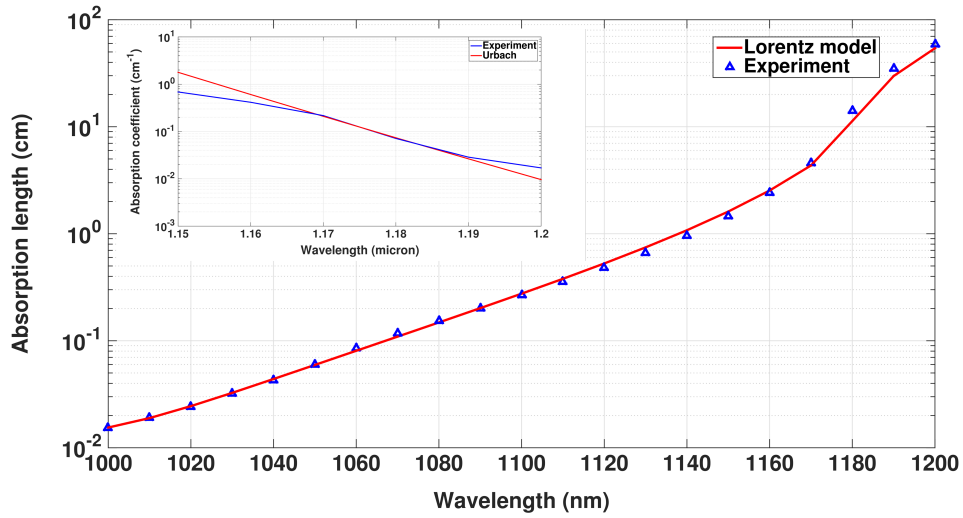

Figure 14. Comparison of absorption lengths obtained from [58] and our fitting function with a series of Lorentz oscillator terms (fitting parameters are given in table II). Inset: Urbach slope exhibited by the experimental absorption coefficient of [58].

To model this behavior, we fit the frequency dependent dielectric constant of Si over the $1000-1200$ nm wavelength range from [58] to a function of the form: $\epsilon(\omega) = \epsilon_\infty + \sum_j \frac{\triangle\epsilon_j \omega_{pj}^2}{\left(\omega_{pj}^2 - 2i\omega\gamma_j - \omega^2\right)}$, where each term of the summation represents a Lorentz oscillator. The fitting parameters ϵ_∞, ω_{pj}, $\triangle\epsilon_j$ and γ_j, used in our FDTD computation, are obtained using an open MATLAB program [59] and are given in table II. Figure 14 compares the absorption length ($\lambda/4\pi k$, where k is

the imaginary part of the refractive index) obtained from our fit to that calculated from [58]. The absorption coefficient of the inverted micro-pyramid PhC is obtained by high-resolution FDTD in the $1100-1200$ nm wavelength range. In order to ensure convergence of the solutions, the FDTD computation are run for sufficiently long time duration and MAPD is finalized only when it shows < 0.01 mA/cm^2 variation over 200 FDTD time-steps. The inset of fig. 6 shows the plot of absorption coefficient for the 10 μm thick inverted micro-pyramid PhC solar cell for $1100-1200$ nm spectral range. The optical absorption over the $1115-1200$ nm wavelength range corresponds to a MAPD of 0.82 mA/cm^2. The calculated optical absorption over the $1100-1200$ nm wavelength range corresponds to a MAPD of 1.09 mA/cm^2 (out of the total available 2.93 mA/cm^2), leading to the overall $J_{MAPD} = 43.59$ mA/cm^2($300-1200$ nm range). The corresponding $J-V$ characteristic is shown by the red curve in fig. 13. Despite the slight drop of V_{OC} owing to BGN, the conversion efficiency of our optimized 10 μm-thick, inverted micro-pyramid, solar cell reaches 30.02%.

VII. SOLAR CELL PERFORMANCE PREDICTIONS AND COMPARISON

In this section, we first compare the effect of sheet resistance on the performances of the $1D$ and $2D$ models of our $10\mu m$-thick inverted pyramid PhC cell. For the $2D$ model, we consider a full-area bottom contact cell (shown in the inset of fig. 15) with $10\mu m$-wide top contacts. The $730nm$-thick emitter and $200nm$-thick BSF of the $2D$ cell are assumed to have Gaussian doping profiles with peak doping concentrations $3\times10^{18}cm^{-3}$ and $2\times10^{19}cm^{-3}$, respectively. The $p-$type bulk has a uniform doping of $5\times10^{15}cm^{-3}$. The SRVs of both top and bottom contacts are $10cm/s$. The surface recombination at the insulator-Si interface is modeled according to eq. 5 with $S_{n0} = 20cm/s$ and $S_{p0} = 1.7cm/s$. The $1D$ transport model has the same doping configurations for the emitter, bulk and BSF as the $2D$ cell. Both the contacts of the $1D$ cell is assumed to have an effective SRV of $10cm/s$. Figure 15 shows the variation with emitter contact finger pitch of the power conversion efficiencies of the $2D$ model and $1D$ transport with sheet-resistance model (eq. 4). As the contact pitch is decreased from $800\mu m$ to $200\mu m$, the conversion efficiency of the $2D$ cell increases from 29.22% to 29.49%. Our combined $1D$ transport and sheet-resistance model captures this trend accurately and predicts the conversion efficiency within an additive factor of 0.1% over the entire range of emitter-pitch.

So far, we have used $\tau_{SRH} = 1.2ms$ in all our simulations. However, measured data (fig. 5 in [4]) shows that typical effective lifetime, $\tau_{eff} = \left({}^{1}/_{\tau_{SRH}} + {}^{1}/_{\tau_{Aug}}\right)^{-1}$, of p-type samples with a doping concentration of $5\times10^{15}cm^{-3}$ is approximately $10ms$. Since $\tau_{SRH} > \tau_{eff}$, it is possible to experimentally obtain $\tau_{SRH} = 10ms$. We re-calculate the $J-V$ parameters of the full-area bottom contact cell with an emitter contact pitch of $500\mu m$ (keeping the doping configurations and SRV models same) under a more realistic situation that includes BGN and $\tau_{SRH} = 10ms$. Figure 16 shows the corresponding $J-V$ curve of the cell, using the $2D$ transport model with exact generation profile, that yields 30.15% power conversion efficiency.

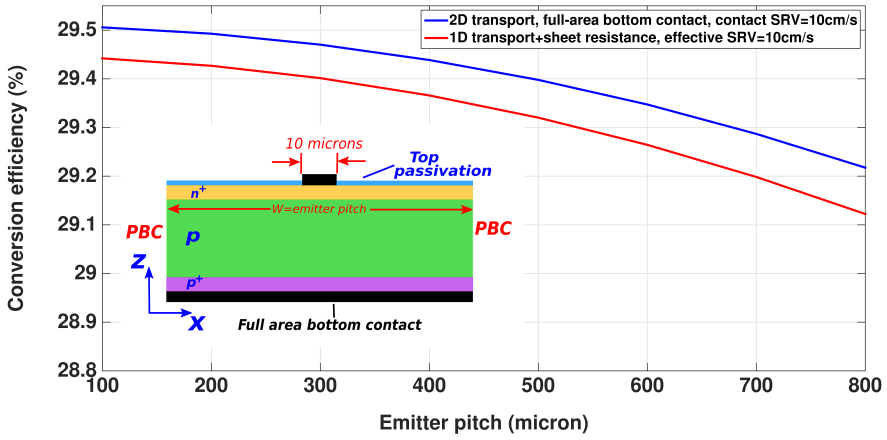

Figure 15. Effect of sheet resistance and top contact finger spacing on efficiency (neglecting BGN). Here, $\tau_{SRH} = 1.2ms$ and top contact fingers are assumed to be cloaked. Blue curve: $2D$ model for the full-area bottom contact, $10\mu m$-thick cell. The $730nm$-thick emitter has a Gaussian doping profile with peak value of $3 \times 10^{18} cm^{-3}$. The $200nm$-thick p^+ BSF has a peak doping of $2 \times 10^{19} cm^{-3}$. The top contact is $10\mu m$ wide. The uniformly doped $p-$type bulk has a doping concentration of $5 \times 10^{15} cm^{-3}$. Both top and bottom contacts are modeled using an effective SRV$= 10cm/s$. The SRV of the insulator-Si interface is determined according to eq. 5 with $S_{n0} = 20cm/s$ and $S_{p0} = 1.7cm/s$. Red curve: $1D$ transport model including sheet-resistance. The $1D$ model has same doping configurations for emitter, bulk and BSF as the $2D$ cell. Effect of sheet resistance is taken into account according to eq. 4. The effective SRV for both the contacts of the $1D$ model is $10cm/s$.

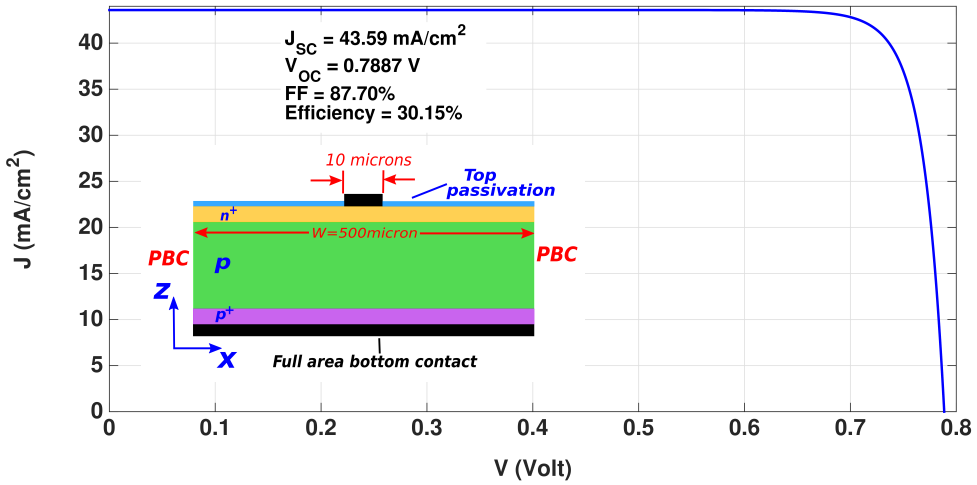

Figure 16. $J - V$ characteristic, calculated by the $2D$ transport model, of full-area bottom contact cell with BGN, $500\mu m$ emitter-pitch and $\tau_{SRH} = 10ms$. The $730nm$-thick emitter of the cell has a Gaussian doping profile with a peak value of $3 \times 10^{18} cm^{-3}$. The $200nm$-thick p^+ BSF has a peak doping of $2 \times 10^{19} cm^{-3}$. The top contact is $10\mu m$ wide. The contact SRVs of top and bottom contacts are $10cm/s$. The SRV of the insulator-Si interface is determined according to eq. 5 with $S_{n0} = 20cm/s$ and $S_{p0} = 1.7cm/s$.

Cell type/ light trapping and transport model	Cell-thickness (μm)	Bulk recombination model	Surface recombination	V_{OC} (V)	J_{SC} (mA/cm^2)	$FF(\%)$	$\eta(\%)$
Hypothetical, undoped/ perfect Lambertian, no BGN	110	Improved Auger [4], $\tau_{SRH} = \infty$	SRV= 0	0.7673	43.31	88.98	29.57
Hypothetical, undoped/ perfect Lambertian, BGN	110	Improved Auger [4], $\tau_{SRH} = \infty$	SRV= 0	0.7613	43.31	89.26	29.43
n^+pp^+ inverted pyramid PhC/ no BGN, $2D$ transport, emitter pitch= $800\mu m$, local bottom contact cell of fig. $22(a)$	10	Improved Auger [4], $\tau_{SRH} = 1.2ms$	Top and bottom contact SRVs $10^3 cm/s$	0.7975	42.5	85.83	29.09
n^+pp^+ inverted pyramid PhC/BGN, $2D$ transport, emitter pitch= $500\mu m$, local bottom contact cell of fig. $22(a)$	10	Improved Auger [4], $\tau_{SRH} = 10ms$	Top and bottom contact SRVs $10^3 cm/s$	0.7815	43.59	87.09	29.8
n^+pp^+ inverted pyramid PhC/ no BGN, $2D$ transport, emitter pitch= $800\mu m$, full-area bottom contact cell of fig. $22(b)$	10	Improved Auger [4], $\tau_{SRH} = 1.2ms$	Top and bottom contact SRVs $10cm/s$	0.7986	42.5	86.09	29.22
n^+pp^+ inverted pyramid PhC/ BGN, $2D$ transport, emitter pitch= $800\mu m$, full-area bottom contact cell of fig. $22(b)$	10	Improved Auger [4], $\tau_{SRH} = 10ms$	Top and bottom contact SRVs $10cm/s$	0.7886	43.59	87.07	29.93
n^+pp^+ inverted pyramid PhC/ BGN, $2D$ transport, emitter pitch= $500\mu m$, full-area bottom contact cell of fig. $22(b)$	10	Improved Auger [4], $\tau_{SRH} = 10ms$	Top and bottom contact SRVs $10cm/s$	0.7887	43.59	87.70	30.15

Table III. Comparison of our inverted pyramid PhC based thin-silicon solar cells with the hypothetical Lambertian solar cell at $25^\circ C$. The inverted pyramid PhC cells employ wave-interference based light trapping. The surface recombination at Si-insulator interfaces of the inverted pyramid PhC cells is modeled according to eq. 5 with $S_{n0} = 20cm/s$ and $S_{p0} = 1.7cm/s$. Our $2D$ transport calculation (that automatically includes the effect of sheet-resistance) with BGN, $\tau_{SRH} = 10ms$ and $500\mu m$ emitter pitch yields a conversion efficiency of 30.15% for a full-area bottom contact cell.

The Lambertian light-trapping based calculations at $25^{\circ}C$ predict upper bounds for a 10 μm cell with $p-$type bulk (doping concentration= $5 \times 10^{15} cm^{-3}$) of $J_{SC} \sim 39.6$ mA/cm^2 and $\eta \sim 28.5\%$ (fig. 4 in [2]). Compared to hypothetical Lambertian cell that ignores the wave nature of light, our inverted micro-pyramid PhC with double layer ARC yields $4mA/cm^2$ higher J_{SC} and 1.6% (additive) higher conversion efficiency. Table III compares the performance parameters of our realistic PhC cell with the performance predicted for the ideal, undoped Lambertian solar cell [2]. The 110 μm thick Lambertian cell is assumed to have perfect AR and no surface recombination.

H (μm)	Required MAPD (mA/cm^2) for $300-1100$ nm wavelength range	V_{OC} (V)	FF (%)
1.6	40.750	0.8318	88.50
3.0	41.348	0.8218	88.27
5.0	41.916	0.8134	87.97
7.0	42.586	0.8045	87.62
10.0	42.862	0.8011	87.35

Table IV. The second column lists the amount of solar absorption required for various thickness, H, of silicon to achieve 30% power conversion efficiency (in absence of BGN) with wave-interference based light-trapping, restricted to the $300-1100$ nm wavelength range. This is calculated in the $1D$ transport model with sheet resistance and $800\mu m$ top contact finger spacing with perfect cloaking. Here, we take $\tau_{SRH} = 1.2ms$. The short circuit current J_{SC} (essentially the same as MAPD in this case), open circuit voltage V_{OC} and fill factor FF are then computed using our optimized doping profile. This listed MAPD requirement is reduced if solar absorption in the $1100-1200$ nm range is included, the value of τ_{SRH} is increased to $10ms$, a $2D$ transport model is used, and/or the emitter contact pitch is reduced to $500\mu m$.

Table IV lists the solar absorption values in MAPD (column 2) required for various thicknesses, H, of crystalline silicon to achieve 30% power conversion efficiency, using the n^+pp^+ doping configuration, from solar absorption restricted to the $300-1100$ nm range. The last three columns show the projected values of short circuit current, open-circuit voltage and fill factor that would result in our model if the required solar absorption is achieved. As shown for the 10 μm-thick case, the inclusion of solar absorption in the $1100-1200$ nm, the use of the more realistic $2D$ transport model, the increase of τ_{SRH} to $10ms$, or the decrease of top-contact finger spacing would relax these listed requirements.

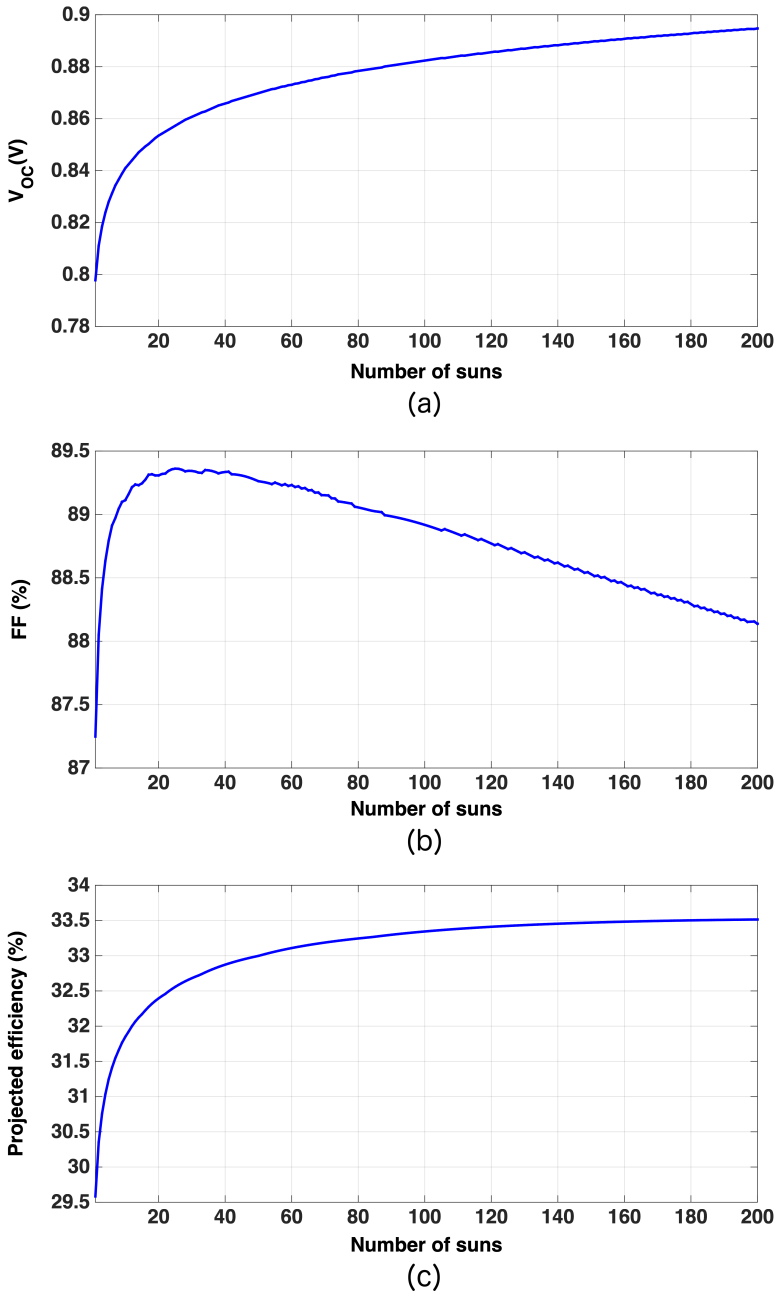

Figure 17. Performance of the 10 μm thick inverted pyramid PhC n^+pp^+ cell under solar concentration at $300K$. Here, solar absorption is restricted to the 300−1100 nm wavelength range, $\tau_{SRH} = 1.2ms$ and contact SRV= $10cm/s$. The power conversion efficiency saturates to 33.5% at 150−suns illumination. This is obtained in a $1D$ electronic transport model neglecting sheet resistance.

We also investigate the performance of our PhC solar cell under solar concentration. With n suns illumination, the MAPD of the concentrator cell is nJ_{MAPD}. The efficiency is determined by the variation of V_{OC} and FF with n (plotted in fig. 17(a) and (b), respectively. For $1 < n \lesssim 20$, V_{OC} increases rapidly due to higher carrier generation. However, the rate of increase of V_{OC} slows down for $n > 30$ as very high excess carrier concentration increases the bulk

Auger recombination rate in the cell. On the other hand, the FF of the cell shows a rapid increase up to $n \approx 20$ and then slowly decreases linearly. Figure 17(c) shows that the conversion efficiency of our concentrator cell reaches 32.5% at $n = 20$ and then slowly saturates to 33.5% for $n \geqslant 150$. A slight improvement in these efficiencies is expected with the addition of solar absorption in the $1100 - 1200nm$ range. In this analysis, we have assumed that the temperature of the cell is maintained at $300K$ through a proper cooling mechanism.

VIII. CONCLUSION

In summary, we have demonstrated a simple photonic crystal solar cell geometry projected to achieve power conversion efficiency beyond previous theoretical bounds for a single junction $c - Si$ solar cell. This was shown with an inverted micro-pyramid PhC that absorbs sunlight beyond the ray-optics based Lambertian limit, through wave-interference based light-trapping. Our FDTD study identifies optimum design parameters for the inverted pyramid PhC and the double layer ARC that enables unprecedented MAPDs in very thin ($3 - 12$ μm) $c - Si$ films owing to long-lifetime photonic resonances in $800 - 1200$ nm spectral range. The order of magnitude reduction of $c - Si$ thickness, compared to the hypothetical 110 μm Lambertian cell and world-record-holding 165 μm Kaneka cell, enables our cell to have an unprecedented $V_{OC} \sim 0.8$ V due to lower bulk-recombination. This is the key factor that enables our photonic crystal solar cell to achieve a projected 30% conversion efficiency. We also demonstrate doping profiles that provide the optimum balance between Auger recombination and FSF/BSF needed to minimize surface recombination. The resulting electronics is similar to that of a "junction-less" solar cell with carrier-selective contacts [56, 57]. The optimum trade-off between solar absorption and bulk-recombination, yields an optimum thickness for the inverted-pyramid PhC solar cell of just 10 μm. This represents a paradigm shift from previous beliefs that the optimum thickness for a silicon solar cell should be close to 110 μm [2] or more [5]. In contrast to standard solar panels, our $10\mu m$-thick silicon photonic crystal sheets are, in principal, flexible and may be used to conformally coat a variety of surfaces such as exterior of buildings.

In addition to describing the optimum situation with $\tau_{SRH} = 10ms$, SRVs on the order of $10cm/s$, optimum doping profiles and ideal contact configurations, we have delineated the way in which power conversion efficiency drops if one or more of these conditions is not satisfied. For example, if the surface recombination velocities exceed $100cm/s$ a noticeable reduction in efficiency occurs. If, in addition, the front and back surface fields are not properly engineered a much dramatic loss in efficiency arises. A reduction in τ_{SRH} to $1.2ms$ typically leads to a 0.5% loss in efficiency. We have also shown the robustness of our inverted micro-pyramid structure to variations in the photonic crystal lattice constant.

$X - Y$ symmetry breaking in photonic crystals has been found to be an effective way to further increase solar absorption in thin-film c—Si cells [60]. Symmetry-breaking of our square-lattice, inverted micro-pyramid PhC may likewise enable further improvement in MAPD over the $300 - 1200nm$ spectral range. Further optimization in wave-interference-based light-trapping is still possible. This would effectively compensate for the indirect bandgap property

of $c-Si$ and enable it to absorb light as if it were a direct bandgap semiconductor. A milestone for any single junction solar cell is the experimental realization of 30% power conversion efficiency. Our study suggests that by including band gap narrowing effects, optimizing doping profiles, realizing $\tau_{SRH} = 10ms$, keeping surface recombination velocities below $100cm/s$, and using a top-contact (cloaked) finger spacing of $500\mu m$, the $10\mu m$-thick photonic crystal $c-Si$ solar cell can achieve this far-reaching goal. The present results provide a useful paradigm for further theoretical and experimental studies of thin-silicon photonic crystal solar cells, combining wave-interference-based solar light-trapping with state-of-the-art electronics.

ACKNOWLEDGEMENTS

This work was supported by the United States Department of Energy DOE-BES in a subcontract under award DE-FGQ2-Q6ER46347.

---

[1] W. Shockley and H. J. Queisser, "Detailed balance limit of efficiency of p-n junction solar cells", J. of Appl. Phys. 32, 510 (1961).

[2] A. Richter, M. Hermle, and S. W. Glunz, "Reassessment of the limiting efficiency for crystalline silicon solar cells", IEEE J. of Photovoltaics 3, 1184 (2013).

[3] T. Tiedje, E. Yablonovitch, G. Cody, and B. Brooks, "Limiting efficiency of silicon solar cells," IEEE Trans. on Electron Devices 31, 711 (1984).

[4] A. Richter, S. W. Glunz, F. Werner, J. Schmidt, and A. Cuevas, "Improved quantitative description of Auger recombination in crystalline silicon", Phys. Rev. B 86, 165202 (2012).

[5] K. Yoshikawa, H. Kawasaki, W. Yoshida, T. Irie, K. Konishi, K. Nakano, T. Uto, D. Adachi, M. Kanematsu, H. Uzu and K. Yamamoto, "Silicon Heterojunction solar cell with interdigitated back contacts for a photoconversion efficiency over 26%", Nature Energy 2, 17032 (2017).

[6] M. A. Green, Y. Hishikawa, E. D. Dunlop, D. H. Levi, J. Hohl-Ebinger and A. W. Y. Ho-Baillie, "Solar cell efficiency tables (version 51)", Prog. Photovolt. Res. Appl. 26, 3 (2018).

[7] A. Chutinan and S. John, "Light trapping and absorption optimization in certain thin-film photonic crystal architectures", Phys. Rev. A 78, 023825 (2008).

[8] S. John, "Strong localization of photons in certain disordered dielectric superlattices", Phys Rev. Lett 58, 2486 (1987).

[9] E. Yablonovitch, "Inhibited spontaneous emission in solid-state physics and electronics", Phys. Rev. Lett. 58, 2059 (1987).

[10] G. Demsey and S. John, "Solar energy trapping with modulated silicon nanowire photonic crystals", J. Appl. Phys. 112, 074326 (2012).

[11] A. Deinega and S. John, "Solar power conversion efficiency in modulated silicon nanowire photonic crystals", J. Appl. Phys. 112, 074327 (2012).

[12] S. Eyderman, S. John and A. Deinega, "Solar light trapping in slanted conical-pore photonic crystals: Beyond statistical ray trapping", J. Appl. Phys. 113, 154315 (2013).

[13] S. Eyderman, S. John, M. Hafez, S. S. Al-Ameer, T. S. Al-Harby, Y. Al-Hadeethi and D. M. Bouwes, "Light-trapping optimization in wet-etched silicon photonic crystal solar cells", J. Appl. Phys. 118, 023103 (2015).

[14] A. Mavrokefalos, S. E. Han, S. Yerci, M. S. Branham and G. Chen, "Efficient Light Trapping in Inverted Nanopyramid Thin Crystalline Silicon Membranes for Solar Cell Applications", Nano Lett., 12, 2792 (2012).

[15] M. S. Branham, W. Hsu, S. Yerci, J. Loomis, S. V. Boriskina, B. R. Hoard, S. E. Han and G. Chen, "15.7% Efficient 10-μm-Thick Crystalline Silicon Solar Cells Using Periodic Nanostructures", Adv. Mater. 27, 2182 – 2188 (2015).

[16] K. Kumar, A. Khalatpour, G. Liu, J. Nogami, and N.P. Kherani, "Converging photo-absorption limit in periodically textured ultra-thin silicon foils and wafers", Solar Energy 155, 1306 (2017).

[17] P. Kuang, S. Eyderman, M. L. Hsieh, A. Post, S. John and S. Y. Lin, "Achieving an Accurate Surface Profile of a Photonic Crystal for Near-Unity Solar Absorption in a Super Thin-Film Architecture", ACS Nano 10, 6116 – 6124 (2016).

[18] M. Ernst, R. Brendel, "Lambertian Light Trapping in Thin Macroporous Silicon Layers", Phys. Status Solidi RRL 8 (2014).

[19] A. Bozzola, M. Liscidini, and L. C. Andreani, "Photonic light-trapping versus Lambertian limits in thin film silicon solar cells with 1D and 2D periodic patterns", Opt. Express 20, $A224 - A244$ (2012).

[20] Z. Yu, A Raman, and S. Fan, "Fundamental limit of nanophotonic light trapping in solar cells", PNAS 107, 17491–17496 (2010).

[21] L. A. Weinstein, W. C. Hsu, S. Yerci, S. Boriskina and G. Chen, "Enhanced absorption of thin- fi lm photovoltaic cells using an optical cavity", J. of Opt. 17, 055901 (2015).

[22] I. Valuev, A. Deinega, A. Knizhnik and B. Potapkin, "Creating Numerically Efficient FDTD Simulations Using Generic C++ Programming", Lecture Notes in Computer Science 4707, 213 (2007).

[23] P. Campbell and M. A. Green, "Light trapping properties of pyramidally textured surfaces", J. of Appl. Phys. 62, 243 (1987).

[24] J. Zhao, A. Wang, and M. A. Green, "24.5% Efficiency Silicon PERT Cells on MCZ Substrates and 24.7% Efficiency PERL Cells on FZ Substrates", Prog. Photovolt: Res. Appl. 7, 471 (1999).

[25] J. Zhao and A. Wang, "Rear emitter $n-$type passivated emitter, rear totally diffused silicon solar cell structure", Appl. Phys. Lett. 88, 242102 (2006).

[26] J. Benick, B. Steinhauser, R. Muller, J. Bartsch, M. Kamp, A. Mondon, A. Richter, M. Hermle, S. Glunz, "High efficiency n-type PERT and PERL solar cells", Proc. of 40^{th} Photovoltaic Specialist Conference (PVSC), 3637 (2014).

[27] W. Cai, S. Yuan, Y. Sheng, W. Duan, Z. Wang, Y. Chen, Y. Yang, P. P. Altermatt, P. J. Verlinden, and Z. Feng, "22.2% Efficiency n-type PERT Solar Cell", Energy Procedia 92, 399 (2016).

[28] F. Kiefer, J. Krugener, F. Heinemeyer, M. Jestremski, H. J. Osten, R. Brendel, R. Peibst, "Bifacial, fully screen-printed n-PERT solar cells with BF_2 and B implanted emitters", Solar Energy Materials and Solar Cells 157, 326 (2016).

[29] A. Schenk, "Finite-temperature full random-phase approximation model of band gap narrowing for silicon device simulation", J. of Appl. Phys. 84, 3684 (1998).

[30] F. Urbach, "The Long-Wavelength Edge of Photographic Sensitivity and of the Electronic Absorption of Solids", Phys. Rev. 92, 1324 (1953).

[31] W. Martienssen, "The optical absorption edge in ionic crystals", Phys. Chem. Solids 2, 257 (1957).

[32] C. H. Grein and S. John, "Temperature dependence of the fundamental optical absorption edge in crystals and disordered semiconductors", Solid State Commun. 70, 87 (1989).

[33] C. H. Grein and S. John, "Temperature dependence of the Urbach optical absorption edge: A theory of multiple phonon absorption and emission sidebands", Phys. Rev. B 39, 1140 (1989).

[34] M. F. Schumann, S. Wiesendanger, J. C. Goldschmidt, B. Blasi, K. Bittkau, U. W. Paetzold, A. Sprafke, R. B. Wehrspohn, C. Rockstuhl, and M. Wegner, "Cloaked contact grids on solar cells by coordinate transformations: designs and prototypes", Optica 2, $850 - 853$ (2015).

[35] M. Langenhorst, M. F. Schumann, R. Schmager, J. Lehr, U. Lemmer, M. Wegener, B. Richards, and U. W. Paetzold, "Performance of Silicon Solar Cells with Cloaked Contact Fingers under Realistic Conditions", Light, Energy and the Environment, OSA Technical Digest (online), $PW2A.3$ (2017).

[36] M. F. Schumann, M. Langenhorst, M. Smeets, K. Ding, U. W. Paetzold, and M. Wegener, "All-Angle Invisibility Cloaking of Contact Fingers on Solar Cells by Refractive Free-Form Surfaces," Adv. Opt. Mater. 1700164 (2017).

[37] E. S. Roman, A. Vitrey, J. Buencuerpo, I. Prieto, J. M. Llorens, A. Garcia-Martin, B. Alen, A. Chaudhuri, A. Neumann, S. R. J. Brueck, and J. M. Ripalda, "Cloaking of solar cell contacts at the onset of Rayleigh scattering", Sci. Rep., 28669 (2016).

[38] `http://fdtd.kintechlab.com/en/download`

[39] A. Deinega and S. John, "Effective optical response of silicon to sunlight in the finite-difference time-domain method," Opt. Lett. 37, 112 (2012).

[40] Synopsys, Synopsys TCAD, release $M - 2016.12$ (2016).

[41] J. Zhao, A. Wang, P. Campbell and M. A. Green, "22.7% Efficient Silicon Photovoltaic Modules with Textured Front Surface", IEEE Tran. on Elec. Dev. 46, $1495 - 1497$ (1999).

[42] H. Y. Chen et al., "Enhanced performance of solar cells with optimized surface recombination and efficient photon capturing via anisotropic-etching of black silicon", Appl. Phys. Lett. 104, 193904 (2014).

[43] M. F. Abdullah, M. A. Alghoul, H. Naser, N. Asim, S. Ahmadi, B. Yatim and K. Sopian, "Research and development efforts on texturization to reducethe optical losses at front surface of silicon solar cell", Renewable and Sustainable Energy Reviews 66, 380–398 (2016).

[44] N. Borojevic, A. Lennon and S. Wenham, "Light trapping structures for silicon solar cells via inkjet printing", Phys. Status Solidi $A211$, 1617–1622 (2014).

[45] H. Y. Chen, H. L. Lu, Q. H. Ren, Y. Zhang, X. F. Yang, S. J. Ding and D. W. Zhang, "Enhanced photovoltaic performance of inverted pyramid-based nanostructured black-silicon solar cells passivated by an atomic-layer deposited Al_2O_3 layer", Nanoscale 7, $15142 - 15148$ (2015).

[46] O. Hohn, N. Tucher and B. Blasi, "Theoretical study of pyramid sizes and scattering effects in silicon photovoltaic module stacks", Opt. Express 26, $A320 - A330$ (2018).

[47] K. Q. Le and S. John, "Synergistic plasmonic and photonic crystal light- trapping: Architectures for optical upconversion in thin-film solar cells", Opt. Express 22, $A1 - A12$ (2014).

[48] E. Yablonovitch, "Statistical ray optics", J. Opt. Soc. Am. 72, $899 - 907$ (1982).

[49] D. Malacara and B. J. Thompson, "Handbook of Optical Engineering", CRC press (2001).

[50] A. Wang, J. Zhao and M. A. Green, "24% efficient silicon solar cells", Appl. Phys. Lett. 57, $602 - 604$ (1990).

[51] `http://www.pveducation.org/pvcdrom/design/emitter-resistance`

[52] PV Lighthouse sheet-resistance calculator, https://www2.pvlighthouse.com.au/calculators/Sheet%20resistance%20calculator/Sheet%20resistance%20calculator.aspx.

[53] A. Cuveas, "Surface recombination velocity of highly doped n-type silicon", J. of Appl. Phys. 80, 3370 (1996).

[54] S. J. Robinson, S. R. Wenham, P. P. Altermatt, A. G. Aberle, G. Heiser and M. A. Green, "Recombination rate saturation mechanisms at oxidized surfaces of high- efficiency silicon solar cells", J. Appl. Phys. 78, 4740 − 4754 (1995).

[55] A. G. Aberle, S. Glunz, W. Warta, "Impact of illumination level and oxide parameters on Shockley-Read-Hall recombination at the $Si - SiO_2$ interface", J. of Appl. Phys. 71, 4422 − 4431 (1992).

[56] F. Feldmann, M. Simon, M. Bivour, C. Reichel, and M. Hermle, "Efficient carrier-selective $p-$ and $n-$contacts for Si solar cells", Solar Energy Materials and Solar Cells 131, 100 (2014).

[57] F. Feldmann, M. Bivour, C. Reichel, M. Hermle, and S. W. Glunz, "Passivated rear contacts for high-efficiency $n-$type Si solar cells providing high interface passivation quality and excellent transport characteristics", Solar Energy Materials and Solar Cells 120, 270 (2014).

[58] C. Schinke, P. C. Peest et al., "Uncertainty analysis for the coefficient of band-to-band absorption of crystalline silicon", AIP Advances 5, 067168 (2015).

[59] http://fdtd.kintechlab.com/en/fitting

[60] S. Bhattacharya and S. John, "Designing high-efficiency thin silicon solar cells using parabolic-pore photonic crystals", Phys. Rev. Applied 9, 044009 (2018).

APPENDIX A

I. Optimization of emitter and BSF

For the sake of comparison with other theoretical models [2], we briefly discuss doping profile optimization, neglecting sheet resistance losses. In the more realistic situation that includes sheet resistance for top contact fingers separated by $800\mu m$, the optimum thickness of the emitter region is increased. In our $1D$ model, this causes a lowering of power conversion efficiency at optimum doping profile by 0.47%. In the $2D$ transport model that automatically includes sheet resistance, the efficiency is reduced by 0.37% from the results described below.

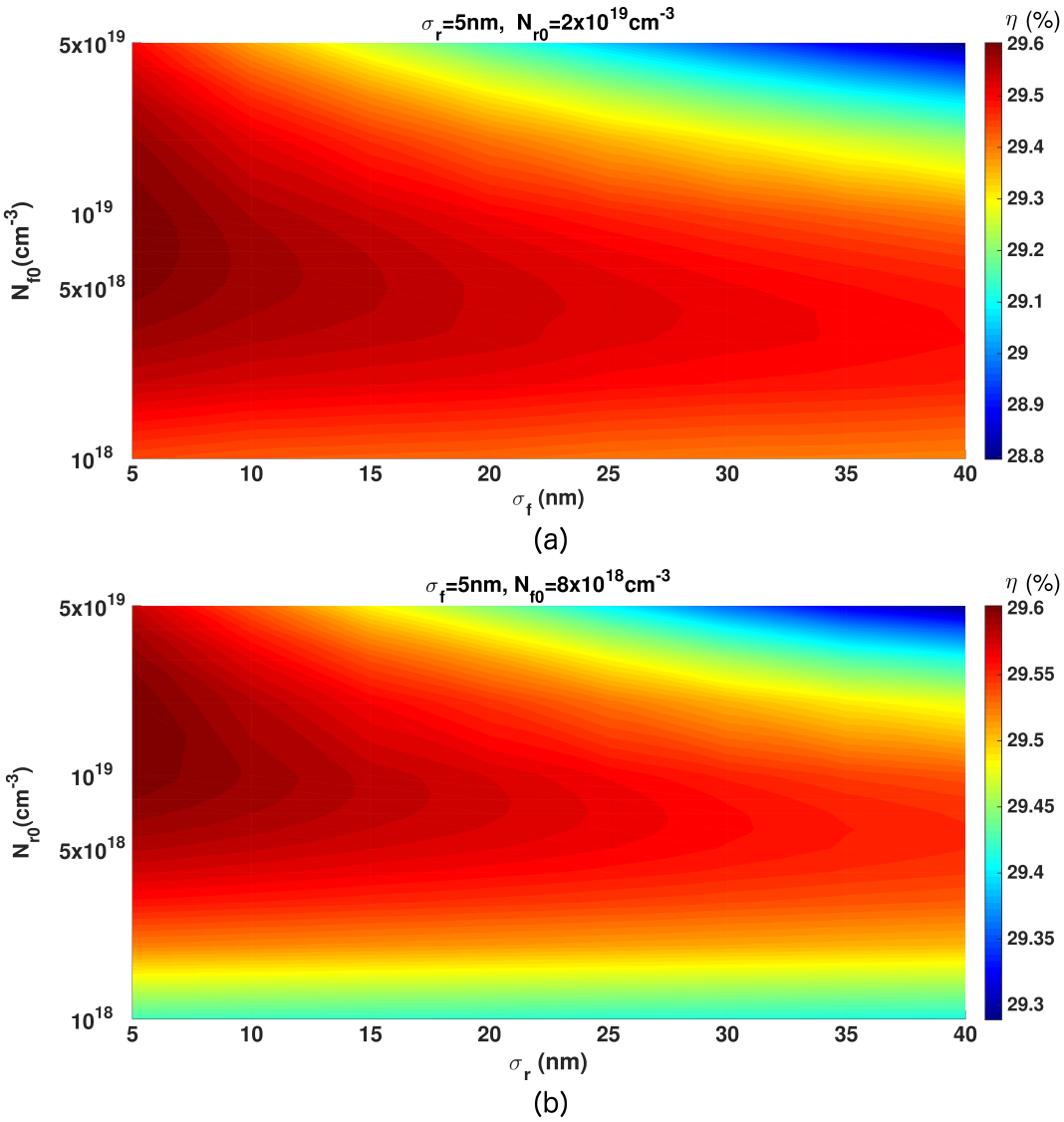

Figure 18. Optimization maps of Gaussian doping profiles in the $1D$ transport model with $\tau_{SRH} = 1.2ms$ and SRV= $10cm/s$, neglecting sheet resistance: (a) front n^+ region (keeping N_{r0} and σ_r fixed) and (b) rear p^+ region (keeping N_{f0} and σ_f fixed). For $\sigma_f = \sigma_r = 5$ nm, the optimum values of N_{f0} and N_{r0} are 8×10^{18} cm^{-3} and 2×10^{19} cm^{-3}, respectively. The modified optimization map, including sheet resistance, is given in fig. 9.

Since the n^+ and p^+ regions are very thin compared to the separation between them, the doping profile of one region does not influence the optimum doping profile of the other. Accordingly, we treat the optimizations of these two regions independently. Figure 18(a) and (b) show the optimization maps for the front n^+ and rear p^+ regions, respectively. As the widths of the regions with high doping are decreased, the optimum values of the peak doping concentration increases. Also, the optimum conversion efficiency steadily rises as we decrease the widths of the n^+ and p^+ regions (equivalently, as σ_f and σ_r decrease). This is an artifact of neglecting sheet resistance. However, a higher doping concentration is necessary for thinner regions in order to maintain sufficient FSF or BSF. Higher doping concentrations tend to increase the Auger recombination in the n^+ and p^+ regions. These two competing processes result in optimum N_{f0} and N_{r0} for a given set of σ_f and σ_r. At $300K$, $\tau_{SRH} = 1.2ms$ and restricting solar absorption

to the $300 - 1100$ nm wavelength range, we obtain the best conversion efficiency of 29.59% for our 10 μm cell with $N_{f0} = 8 \times 10^{18}$ cm^{-3}, $\sigma_f = 5$ nm, $N_{r0} = 2 \times 10^{19}$ cm^{-3} and $\sigma_r = 5$ nm (the corresponding widths of the n^+ and p^+ regions are ~ 20 nm) in comparison to the 29.57% conversion efficiency of the hypothetical Lambertian cell that uses $\tau_{SRH} \to \infty$ and neglects surface recombination [2]. Figure 18(a) shows that when σ_r is kept fixed at 5 nm, reducing σ_f from 35 to 5 nm causes $\sim 0.1\%$ increase in the optimum conversion efficiency. On the other hand, fig. 18(b) shows that a similar reduction in σ_r (keeping σ_f fixed at 5 nm) increases the conversion efficiency by $\sim 0.05\%$. Thus, the width of the front n^+ layer has a higher influence on the efficiency than that of the rear p^+ layer. In any event, there is a broad range of Gaussian doping profiles for which the power conversion efficiency remains above 29%. Our Sentaurus calculations with cell-thicknesses $H = 3$, 5, 7 and 12 μm reveal that the optimum doping profiles are the same in each case.

II. Comparison with optimized n^+p solar cell

The classic $p-n$ junction solar cell with moderately high doping throughout the bulk suffers considerable loss from bulk non-radiative carrier recombination. This is overcome by a profile with low doping throughout the bulk and high doping n^+ and p^+ regions relegated to thin regions near the top and bottom contacts.

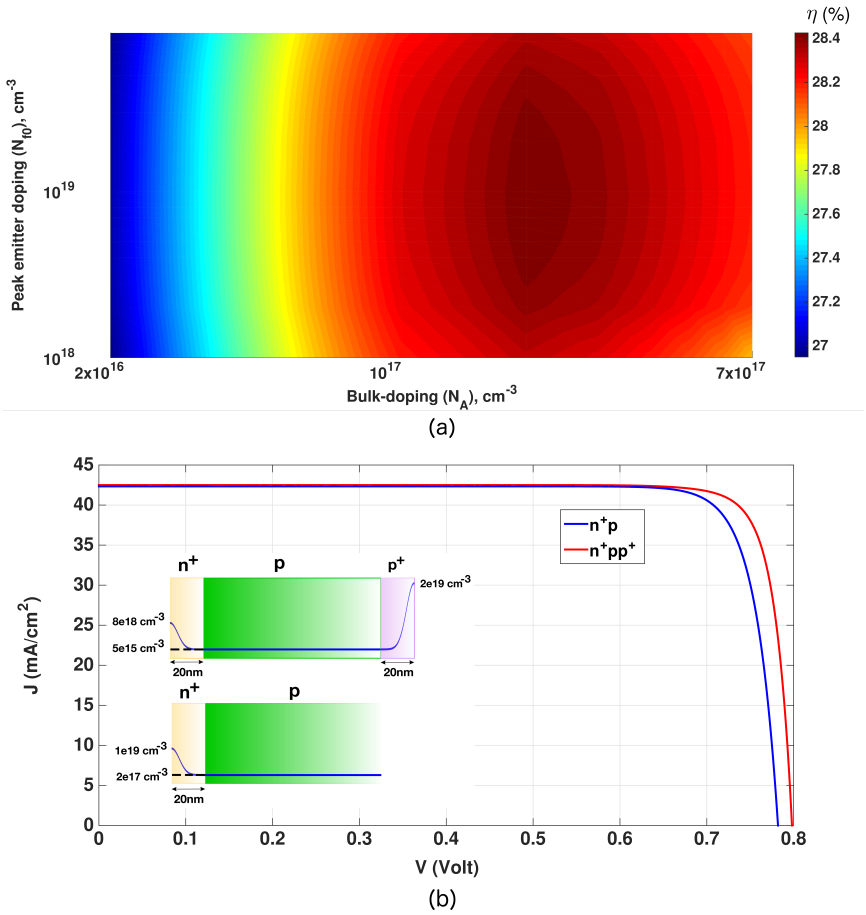

Figure 19. (a) Doping optimization for n^+p cell using a $1D$ transport model, neglecting sheet resistance: the 20 nm n^+ emitter has a Gaussian doping profile and the $p-$type bulk has a uniform doping. (b) Comparison of $J-V$ characteristics of the n^+pp^+ and n^+p cells at $300K$, assuming MAPD of 42.5 mA/cm^2 from solar absorption in the $300-1100$ nm range. The inset shows the doping profiles used for both cells. In both cases, we assume $\tau_{SRH}=1.2ms$ and $SRV=10cm/s$ for top and bottom contacts.

In order to illustrate the importance of doping profile, we compare our optimized n^+pp^+ cell with an optimized, 10 μm n^+p cell having the same carrier generation profile. Here, we use a $1D$ transport model, neglecting sheet resistance, assuming $\tau_{SRH}=1.2ms$ and $SRV=10cm/s$ at both contacts. Figure 19(a) illustrates the doping profile optimization of the n^+p cell. This shows that the conversion efficiency for the n^+p cell reaches a maximum value of 28.43% for $N_D=1\times10^{19}$ cm^{-3} and $N_A=2\times10^{17}$ cm^{-3}. In fig. 19(b), we compare the $J-V$ characteristics of both the cells. For the n^+p cell, $\eta=28.43\%$, $J_{SC}=42.33$ mA/cm^2, $V_{OC}=0.782$ V and $FF=85.86\%$ whereas for the n^+pp^+ cell $\eta=29.59\%$, $J_{SC}=42.497$ mA/cm^2, $V_{OC}=0.798$ V and $FF=87.23\%$. The n^+pp^+ cell has 1.2% higher conversion efficiency due to reduced Auger recombination in the bulk and reduced surface recombination due to the stronger p^+ BSF. The ultra-thin architecture of the heavily doped regions helps to minimize Auger recombination in the FSF and BSF regions.

APPENDIX B

I. Comparison of $1D$, $2D$ and $3D$ Transport Models of $H = 3\mu m$ Cell

As a first step towards validating our $1D$ transport results, we consider a $3\mu m$-thick inverted pyramid PhC cell. First, we show that for this thin cell, $3D$ and $2D$ carrier transport calculations yield the same results for both low and high values of contact recombination velocities. We also show that the results of the $2D$ and $3D$ transport models, which already include the effect of sheet-resistance, are in close agreement with our $1D$ transport model that separately accounts for sheet-resistance through P_{loss} (described in sec. V). In section II of this appendix, we consider $2D$ transport calculations of $10\mu m$-thick cell and show that the $2D$ model provides a very slight enhancement in efficiency relative to the $1D$ model with sheet-resistance. This suggests that essential parameters such as, bulk and surface recombination are reasonably taken into account in our $1D$ transport model through an effective SRV and that actual performance is at least as good as this model predicts. In section III, we provide a comparison between actual and equivalent $1D$ photo-carrier generation profiles. We also compare the efficiencies of full back contact and local back contact in the $2D$ transport model.

The optimized $3\mu m$-thick $3D$ inverted-pyramid PhC cell has a $1.3\mu m$ lattice constant. The conformal n^+ emitter region is $730nm$ thick and has a Gaussian doping profile with a peak value of $3\times10^{18}cm^{-3}$. The full-area, $200nm$-thick p^+ BSF has a Gaussian doping profile with a peak value $2\times10^{19}cm^{-3}$. The $3D$ transport model of the cell includes the effects of the inverted-pyramid texture shown in fig. 1. The lateral flow of current is calculated and depicted in fig. 21. For this validation we choose the top and local bottom contact width as $10\mu m$. These contacts extend throughout the cell-length along y-direction. The $2D$ counterpart of this $3D$ cell is assumed to have a planar top-surface and the same configurations for doping profiles and contacts (shown in inset of fig. 20). The dimension of the unit cell used in the $3D$ transport calculation is $260\mu m\times260\mu m$ (i.e. 200×200 inverted-pyramid PhC unit-cells). Periodic boundary condition is applied along $x-$direction for both $2D$ and $3D$ models. The $2D$ counterpart of the $3D$ model is $260\mu m$ wide. The unit cells for both $2D$ and $3D$ transport calculations contain three equidistant base-contacts. Thus, the emitter and base contact pitches are $260\mu m$ and $86.5\mu m$, respectively. An equivalent $1D$ generation profile obtained using the algorithm of sec. II yields a MAPD of $39.05mA/cm^2$ (as shown in table I).

For all the $3D$ and $2D$ computations, we use SRH statistics for the insulator-Si interface. In this model, the recombination rate at the Si-insulator interface can be calculated as [53]:

$$R_{surface}^{SRH} = \frac{\left(n_s p_s - n_i^2\right)}{{}^{(n_s+n_i)}/_{S_{p0}} + {}^{(p_s+n_i)}/_{S_{n0}}} \tag{5}$$

where, $S_{j0} = v_{th,j}\sigma_j D_{interface}$ with $j = n, p$ ($v_{th,j}$ is the thermal velocity, σ_j is the capture cross-section, $D_{interface}$ is the interface trap density at the oxide-semiconductor interface), n_s and p_s are electron and hole concentration at Si surface, $n_i = \sqrt{N_e N_h}\exp\left(-{}^{E_g(T)}/_{2k_BT}\right)$. Here, T is the temperature (in K) and $E_g(T)$ denotes the bandgap of

Si. N_e and N_h are defined in terms of the electron/hole effective mass m_e^*/m_h^* and Planck's constant h as: $N_j = 2\left(\frac{2\pi m_j^* K_B T}{h^2}\right)^{3/2}$ with $j = e$ and h for electrons and holes, respectively. For electrons, $v_{th} = \sqrt{\frac{3KT}{m_e^*}} = 1.12 \times 10^7 cm/s$ for $m_e^* = 1.08 m_e$ and T=298K. For holes, v_{th} would be slightly lower due to higher effective mass ($\sim 1.5 m_e^*$). For the rear oxide surface of a cell with local back contacts, the measured value of the near-midgap trap density at the Si-insulator interface, $D_{interface} = 3 \times 10^9 cm^{-2}$ (table I in [54]). From the survey of published data on capture cross-sections (fig. 6 in [55]), $\sigma_p = 6 \times 10^{-17} cm^2$ for these traps. The same figure shows that measured value of σ_n varies over a large range. The choice of $\sigma_n = 6 \times 10^{-16} cm^2$ results in a S_{n0} that closely approximates the effective SRV of the state of the art measurements in [4]. Accordingly, we choose $S_{n0} \approx 20.16 cm/s$ and $S_{p0} \approx 1.7 cm/s$.

For the metal-Si interface, we consider two different cases with effective contact SRVs $10 cm/s$ and $10^6 cm/s$. The $J - V$ curves corresponding to the $2D$ and $3D$ models of the $3\mu m$-thick cell for each choice of contact SRVs are shown in fig. 20. This comparison shows that the $2D$ and $3D$ transport models of the $3\mu m$-cell agree well for both good and bad contact SRVs. For contact SRV= $10 cm/s$, the $2D$ and $3D$ models yield 27.15% and 27.26% power conversion efficiencies, respectively. The corresponding values for contact SRV= $10^6 cm/s$ are 19.47% and 19.43%, respectively. A summary of the $1D$, $2D$ and $3D$ transport results for the $3\mu m$-thick cell in table V shows that the conversion efficiency predicted by $1D$ model with sheet resistance is only 0.2% higher than the $3D$ model for contact SRV= $10 cm/s$ where as, for a higher contact SRV, the equivalent $1D$ model yields the same conversion efficiency as the $3D$ model. The $1D$ model is assumed to have the same doping configurations for the bulk, emitter and BSF as the $2D$ and $3D$ cells. In the model, the power loss due to sheet resistance is calculated using eq. 4 with emitter finger spacing $S = 260\mu m$. For the $3D$ transport calculations, we plot in fig. 21 the spatial profiles of current density at the maximum power point of the $J - V$ curve ($V = 0.7283V$) with contact SRV= $10 cm/s$ (corresponding to blue, solid $J - V$ curve in fig. 20). Figure 21(c) shows the plot of the current-density vector field over a volume of the cell. The current near the textured top surface is dominated by its x-component. For the rest of the cell, current mainly flows along z-direction.

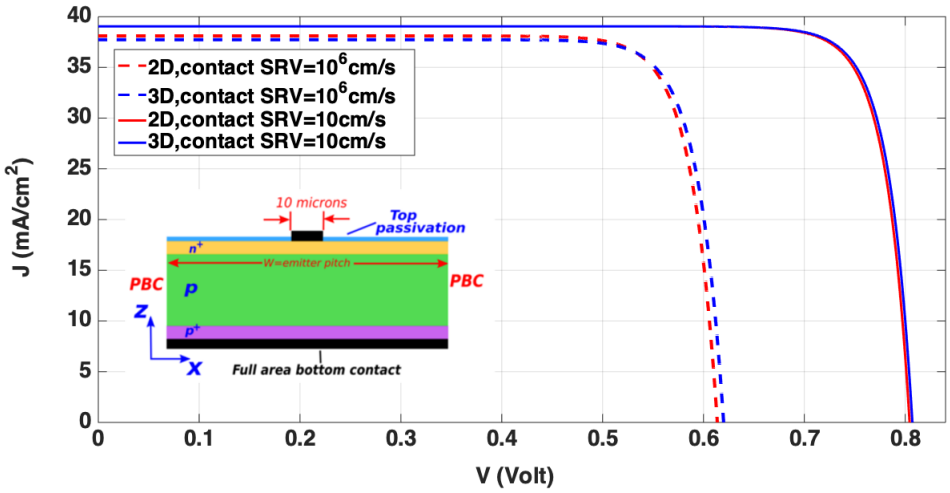

Figure 20. $2D$ and $3D$ carrier transport calculations of $3\mu m$-thick inverted pyramid PhC solar cell with $\tau_{SRH} = 1.2ms$ for low and high surface recombination velocities of the front and rear contacts. The $3D$ cell is textured with inverted pyramid PhC with $1.3\mu m$ lattice constant. The conformal $730nm$-thick emitter has Gaussian doping profile with a peak value of $3\times10^{18}cm^{-3}$. The $200nm$-thick p^+ BSF has a peak doping of $2 \times 10^{19}cm^{-3}$. The top surface of the $2D$ cell is assumed to be planar (shown in the inset) and its emitter and BSF have the same configurations as the $3D$ cell. The unit cell for $3D$ transport calculation is $260\mu m \times 260\mu m$ with periodic boundary condition (PBC) along $x-$direction. The unit cell for $2D$ calculation is $260\mu m$ wide with PBC along $x-$direction. For both $2D$ and $3D$, the top contact finger width is $10\mu m$ with a pitch of $260\mu m$.

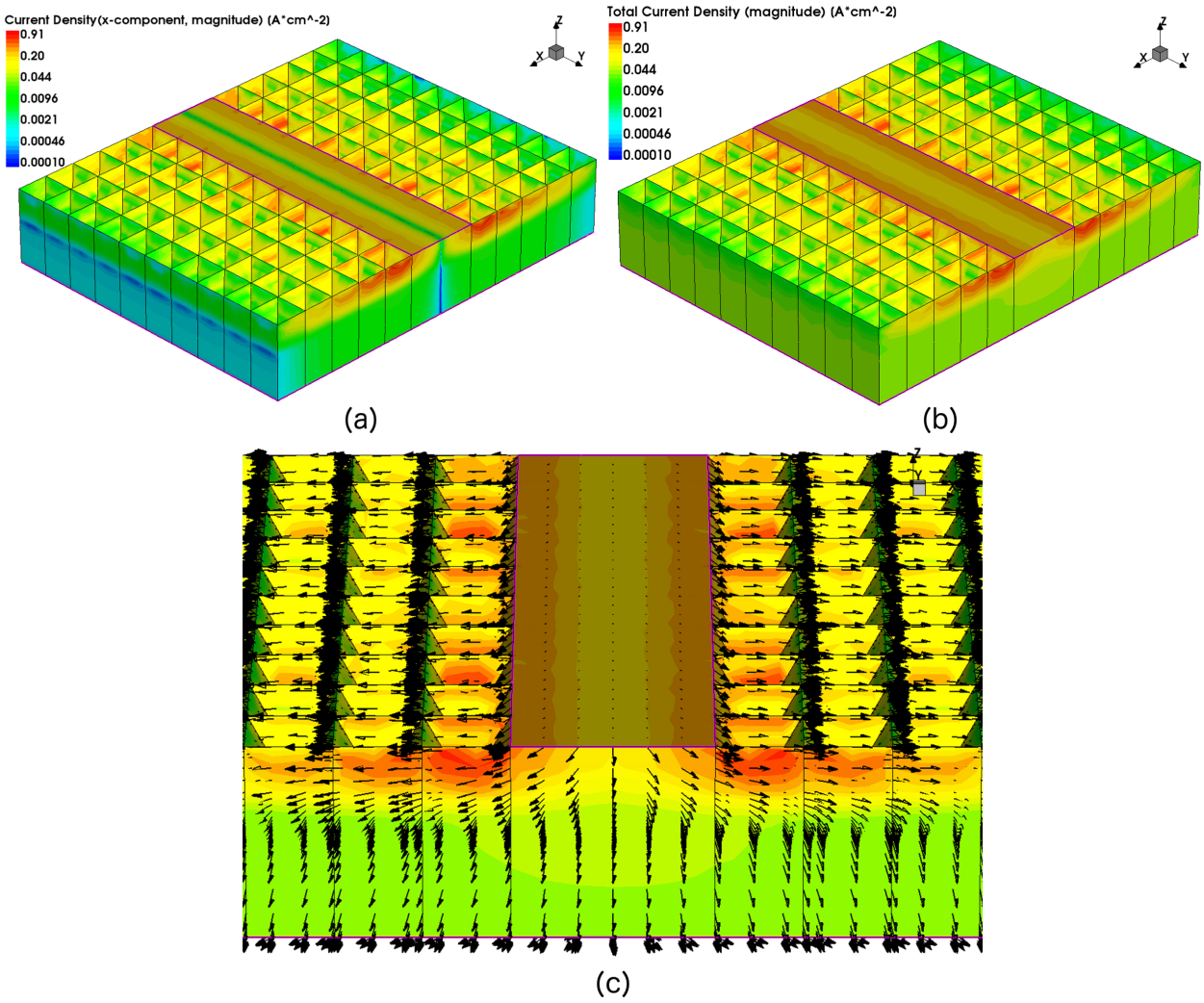

Figure 21. $3D$ carrier transport in $3\mu m$-thick inverted pyramid PhC solar cell with full area back-contact, $\tau_{SRH} = 1.2ms$ and contact SRV$= 10cm/s$: (a) magnitude of x-component of current density and (b) magnitude of total current density, both plotted at the maximum power point. (c) Plot of the current density vector field superposed on total current density plot. The flow of negatively charged electrons is opposite to the arrows. (b) and (c) have the same scale for the colorbar. The $3D$ cell is textured with inverted pyramid PhC with $1.3\mu m$ lattice constant. The conformal $730nm$-thick emitter has Gaussian doping profile with a peak value of $3 \times 10^{18} cm^{-3}$. The $200nm$-thick p^+ BSF has a peak doping of $2 \times 10^{19} cm^{-3}$. The unit cell for $3D$ transport calculation is $260\mu m \times 260\mu m$ with periodic boundary condition (PBC) along x and $y-$directions. The top contact finger width is $10\mu m$ with a pitch of $260\mu m$. Lateral current flow is very prominent in the vicinity of the textured region near the top as electrons flow toward the top contact.

Transport model	Contact SRV (cm/s)	J_{SC} (mA/cm^2)	V_{OC}(V)	$FF(\%)$	Fraction of power loss due to sheet resistance(%)	$\eta(\%)$
$1D$+ sheet resistance	$10cm/s$	39.04*	0.8108*	86.872*	0.1053	27.47
$2D$	$10cm/s$	39.04	0.8044	86.434	–	27.15
$3D$	$10cm/s$	39.04	0.8072	86.519	–	27.27
$1D$+ sheet resistance	$10^6cm/s$	38.95*	0.6041*	82.802*	0.0014	19.47
$2D$	$10^6cm/s$	38.10	0.6138	83.074	–	19.43
$3D$	$10^6cm/s$	37.73	0.6200	83.213	–	19.47

Table V. Comparison of $1D$, $2D$ and $3D$ transport models of $3\mu m$-thick inverted pyramid PhC cell with $\tau_{SRH} = 1.2ms$, excluding BGN. The $2D$ and $3D$ transport model already includes the effect of sheet resistance. Effect of sheet resistance is taken into account in the $1D$ model through direct calculation of power loss at maximum power point according to eq. 4. *Since this sheet resistance model does not predict V_{OC}, J_{SC} or FF, the corresponding entries are those prior to the inclusion of sheet resistance loss.

II. Comparison of $1D$ and $2D$ Transport Models of $H = 10\mu m$ Cell

In this section, we compare the results of our $1D$ and $2D$ transport models for a $10\mu m$-thick cell with full-area back contact. It is shown that the more precise $2D$ transport model predicts an efficiency 0.1% greater than the $1D$ transport model with sheet resistance separately accounted for.

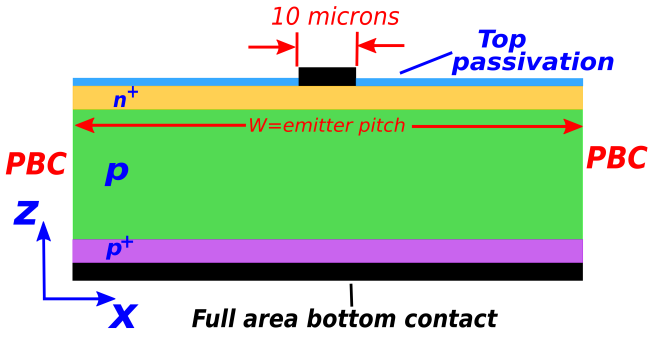

Figure 22. 2D transport model of $10\mu m$-thick, full-area bottom-contact cell. The $730nm$-thick emitter of the cell has a Gaussian doping profile with a peak value of $3 \times 10^{18}cm^{-3}$. The $200nm$-thick p^+ BSF has a peak doping of $2 \times 10^{19}cm^{-3}$. The top contact is $10\mu m$ wide. The width (W) of the unit cell for transport calculation is equal to the emitter pitch, $800\mu m$. The contact SRVs of top and bottom contacts are $10cm/s$. The SRV of the insulator-Si interface is determined according to eq. 5 with $S_{n0} = 20cm/s$ and $S_{p0} = 1.7cm/s$. Here, we choose $\tau_{SRH} = 1.2ms$.

The geometry of the $2D$ transport model of the $10\mu m$-thick inverted pyramid PhC cell with full-area back contact is shown in fig. 22. The dimension of the unit cell used in our $2D$ transport calculation is determined by the emitter-pitch. We apply periodic boundary condition along $x-$direction. The cell employs $730nm$-thick emitter and $200nm$-thick p^+ BSF with Gaussian doping profiles. The peak doping concentrations for emitter and BSF are $3\times10^{18}cm^{-3}$ and $2\times10^{19}cm^{-3}$, respectively. The bulk $p-$region has a uniform doping concentration of $5\times10^{15}cm^{-3}$. The top contact width is $10\mu m$. The contact SRVs for both top and bottom contacts are assumed to be $10cm/s$. The

carrier recombination at the Si-insulator surface is described according to the SRH model of eq. 5 with $S_{n0} = 20cm/s$ and $S_{p0} = 1.7cm/s$. For a fixed emitter contact-finger pitch of $800\mu m$, we show the comparison between the $J-V$ parameters of the $2D$ and $1D$ models in table VI. Our $1D$ equivalent model with an effective SRV of $10cm/s$, along with the sheet resistance loss (according to eq. 4), underestimates the efficiency of the $2D$ model by an additive factor of 0.1%.

III. Local-area Back Contact Cell

We consider an alternative $2D$ cell geometry with local-area back contacts in fig. 23. The emitter contact finger pitch is $800\mu m$ where as the bottom contact-pitch is $266.5\mu m$. The $2D$ transport calculation is performed with periodic boundary condition and a unit cell consisting of 320 photonic-crystal unit cells, spanning $800\mu m$. Both top and bottom contacts are $10\mu m$ wide and have SRVs $1000cm/s$. The $730nm$-thick emitter of the cell has a Gaussian doping profile with a peak value of $3\times10^{18}cm^{-3}$. The $200nm$-thick p^+ BSF has a peak doping of $2\times10^{19}cm^{-3}$. The SRV of the insulator-Si interface is determined according to eq. 5 with $S_{n0} = 20cm/s$ and $S_{p0} = 1.7cm/s$. Here, we choose $\tau_{SRH} = 1.2ms$. The $J-V$ parameters of this cell from table VI illustrate that it is possible to have a higher contact SRV and still design a cell that is able to achieve similar conversion efficiency as our full-area back contact $2D$ model and $1D$ model.

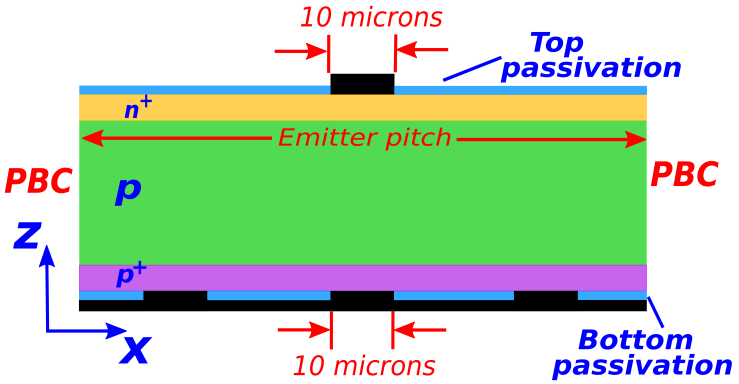

Figure 23. 2D transport model of local-area bottom contact $10\mu m$-thick cell. The unit cell for transport calculation is $800\mu m$ wide and has one top contact and 3 equidistant bottom contacts. Both top and bottom contacts are $10\mu m$ wide and have SRVs $1000cm/s$. The $730nm$-thick emitter of the cell has a Gaussian doping profile with a peak value of $3\times10^{18}cm^{-3}$. The $200nm$-thick p^+ BSF has a peak doping of $2\times10^{19}cm^{-3}$. The SRV of the insulator-Si interface is determined according to eq. 5 with $S_{n0} = 20cm/s$ and $S_{p0} = 1.7cm/s$. Here, $\tau_{SRH} = 1.2ms$.

The last two rows of table VI compare the performance parameters of the local-area bottom contact cell obtained using the equivalent carrier generation profile (calculated according to the algorithm described in sec. II) to that obtained by using the actual integrated carrier generation profile of fig. $5(e)$. The carrier generation rate is repeated over 320 unit cells of the PhC to cover the $800\mu m$ separation of the $10\mu m$-wide front contacts. The performance parameters corresponding to both the carrier generation profiles show excellent agreement, both yielding a power

conversion efficiency of 29.09%.

Transport model	Contact SRV (cm/s)	J_{SC} (mA/cm^2)	V_{OC}(V)	FF(%)	Fraction of power loss due to sheet resistance(%)	η(%)
$1D$, with sheet resistance, equivalent generation profile	$10cm/s$	42.5*	0.7998*	87.402*	1.103	29.12
$2D$, full-area bottom contact, equivalent generation profile	$10cm/s$	42.5	0.7986	86.085	–	29.22
$2D$, local-area bottom contact, equivalent generation profile	$10^3cm/s$	42.5	0.7975	85.831	–	29.09
$2D$, local-area bottom contact, actual generation profile	$10^3cm/s$	42.5	0.7975	85.827	–	29.09

Table VI. Comparison of $2D$ and $1D$ transport model for $10\mu m$-thick cell with $\tau_{SRH} = 1.2ms$ excluding BGN. The power loss in the $1D$ model due to sheet resistance is accounted for using eq. 4. Since, this sheet resistance model directly calculates the power loss at maximum power point and does not predict V_{OC}, J_{SC} or FF, the corresponding entries * are those prior to the inclusion of sheet resistance loss. The $J-V$ parameters, obtained using the actual integrated generation profile, are found to be the same as those obtained using the equivalent generation profile (calculated according to the algorithm described in sec. II). Both full-area and local-area bottom contact configurations are found to be in reasonable agreement with $1D$ transport model that takes into account sheet resistance.